J Adv Ceram

Review

Engineering design of feedstock powder and relevant thermal–mechanical performance of thermal/environmental barrier coatings

Xinchang Feng[1], Fangwei Guo[1,2]✉, Lirong Luo[1], Yuzhang Wang[3], Yun Long[4], Xiaofeng Zhao[1], Fei Pan[5], Lei Guo[6], Qingfeng Zeng[7], Jing Feng[8], Chunlei Wan[9]

Cite this article: Feng X, Guo F, Luo L, et al. *J Adv Ceram* 2025, **14**(2): 9221033. https://doi.org/10.26599/JAC.2025.9221033

ABSTRACT: The development of aeroengine with a high thrust-weight ratio poses great challenges for current top-coating thermal barrier coatings (TBCs) and environmental barrier coatings (EBCs) in service. Medium/high-entropy ceramics are highly promising candidate material for advanced TBCs/EBCs owing to their low thermal conductivity, high melting point, high-temperature stability, and calcium–magnesium–alumino–silicate (CMAS) resistance. Most feedstock powder used for medium/high-entropy TBCs/EBCs is prepared via traditional spray drying, which cannot fully exploit the advantages of multicomponent ceramics. The density, sphericity, inner structure, and flowability of feedstock powder affect their melting state during the thermal spraying process, which strongly affects the microstructure and properties of the deposited coatings. Therefore, the deposited coatings exhibit phase segregation, amorphous phases, and microstructure defects owing to unpredictable variations in feedstock powder with random morphologies and structures. Here, the structure and properties of feedstock powder prepared by state-of-the-art granulation technologies and their influences on the deposited coatings were systematically investigated, which can provide guidance for configuration optimization of feedstock powder and the manufacturing accuracy of the deposited coating. This review aims to bridge the gap between cutting-edge ceramics and advanced engineering technologies, thus providing concrete background knowledge and crucial guidelines for designing and developing TBCs/EBCs.

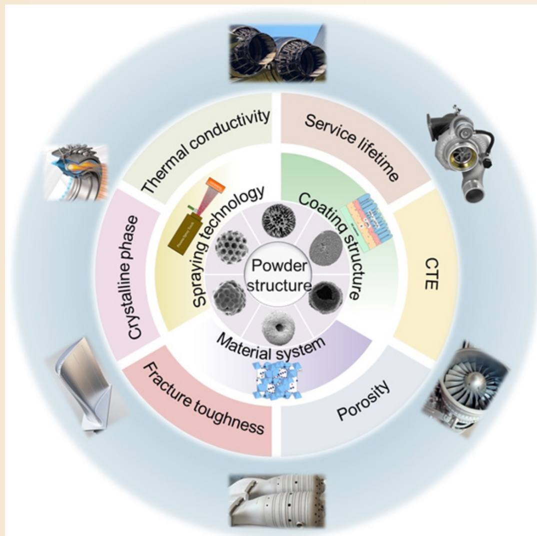

KEYWORDS: thermal/environmental barrier coatings (TBCs/EBCs); spraying ceramic powder; multiscale structure control; high-entropy ceramics; thermal-mechanical performance

1 Introduction

By 2024, the global thermal spraying market is approximately 14.21 billion and is expected to grow at a compound annual growth rate of 7.3% from 2024 to 2029 [1]. Figure 1(a) of publications on thermal spraying in the last 20 years obtained from Web of Science also illustrates the rapid development of thermal spraying. The main applications of thermal spraying material and technologies include thermal barrier coatings (TBCs) and environmental barrier coatings (EBCs), which are critical for advanced aeroengines and gas turbines (Fig. 1(b)).

The increasing demand for fourth-generation high-performance aeroengines has promoted the development of novel material and manufacturing technologies based on lightweight SiC_f/SiC ceramic matrix composites (CMCs) [2–4]. Although

[1] Shanghai Key Laboratory of Advanced High-temperature Materials and Precision Forming, School of Materials Science and Engineering, Shanghai Jiao Tong University, Shanghai 200240, China. [2] National Engineering Research Center of Special Equipment and Power System for Ship and Marine Engineering, Shanghai 200030, China. [3] School of Mechanical Engineering, Shanghai Jiao Tong University, Shanghai 200240, China. [4] State Key Laboratory of Advanced Nuclear Energy Technology, Nuclear Power Institute of China, Chengdu 610213, China. [5] Innovative Sensor Technology IST AG, Ebnat-Kappel 9642, Switzerland. [6] School of Materials Science and Engineering, Tianjin University, Tianjin 300072, China. [7] Tianmushan Laboratory, Hangzhou 311115, China. [8] School of Materials Science and Engineering, Kunming University of Science and Technology, Kunming 650093, China. [9] State Key Laboratory of New Ceramics and Fine Processing, School of Materials Science and Engineering, Tsinghua University, Beijing 100084, China.

✉ Corresponding author. E-mail: fwguo2014@sjtu.edu.cn

Received: October 19, 2024; Revised: January 7, 2025; Accepted: January 8, 2025

CMCs possess high-temperature stability, a low coefficient of thermal expansion (CTE), and excellent mechanical properties, they are more vulnerable to harsh service environments, including water vapor corrosion and the corrosion of various molten salt impurities [5–7], resulting in the rapid consumption of CMCs. To solve this problem, it is necessary to prepare EBCs on the surface of CMCs in addition to applying TBCs [8–10]. National Aeronautics and Space Administration (NASA) reported that the service temperature of ceramic top coats gradually increases from 1315 to more than 1480 ℃ [11]. The multilayer structural TBC/EBC proposed by NASA is an effective measure to increase the service temperature and is composed of a ceramic top coat TBC with good thermal insulation and an inner coat EBC resistant to high-temperature water vapor corrosion (Fig. 2) [12–15]. However, the CTE mismatch and chemical compatibility between TBCs and EBCs or between EBCs and CMCs usually lead to premature cracking failure of the coating. Although introducing an intermediate layer can alleviate the problem of CET mismatch to a certain extent, there are still some inevitable problems, such as poor binding strength, a temperature gradient, and adverse reactions at high temperatures [10]. Therefore, the future trend is the development of one-material dense TBCs/EBCs with low thermal conductivity, good CTE matching with CMCs, excellent high-temperature stability, and resistance to water vapor and CMAS corrosion [16–22]. However, it is difficult to optimize multiple properties at the same time through existing preparation methods to meet the diversity of T/EBC performance requirements. The main goals of new TBCs/EBCs are to search for

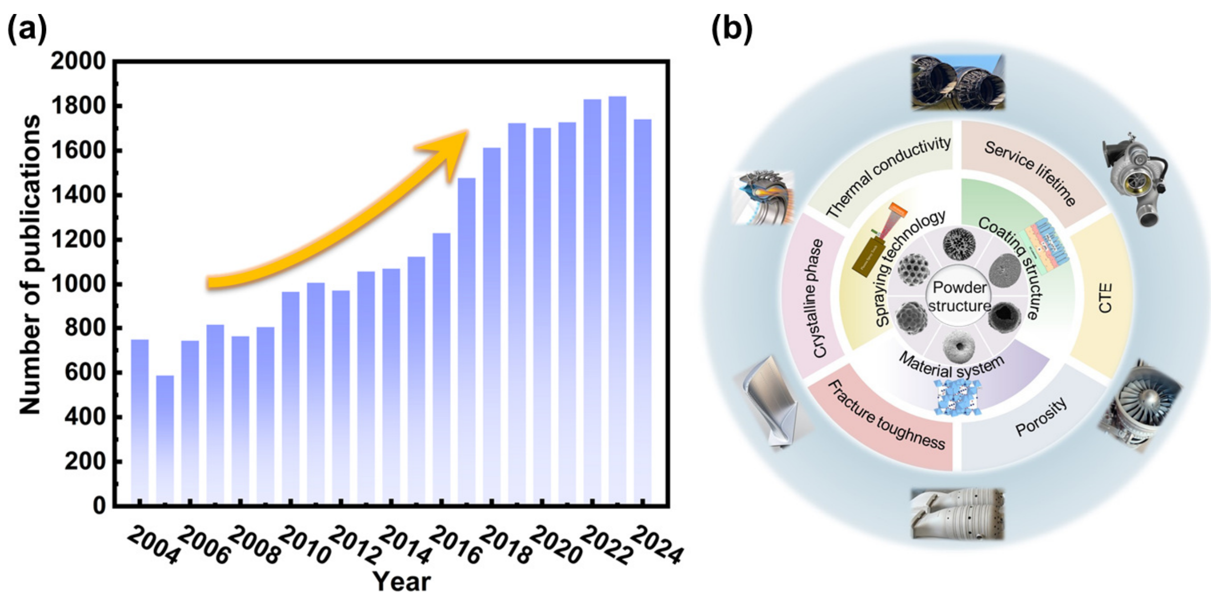

Fig. 1 (a) Global trend of published papers on thermal spraying in the past 20 years (cited from Web of Science). (b) Feedstock powder with different structures and their effects on the performance of the top coat of TBCs/EBCs.

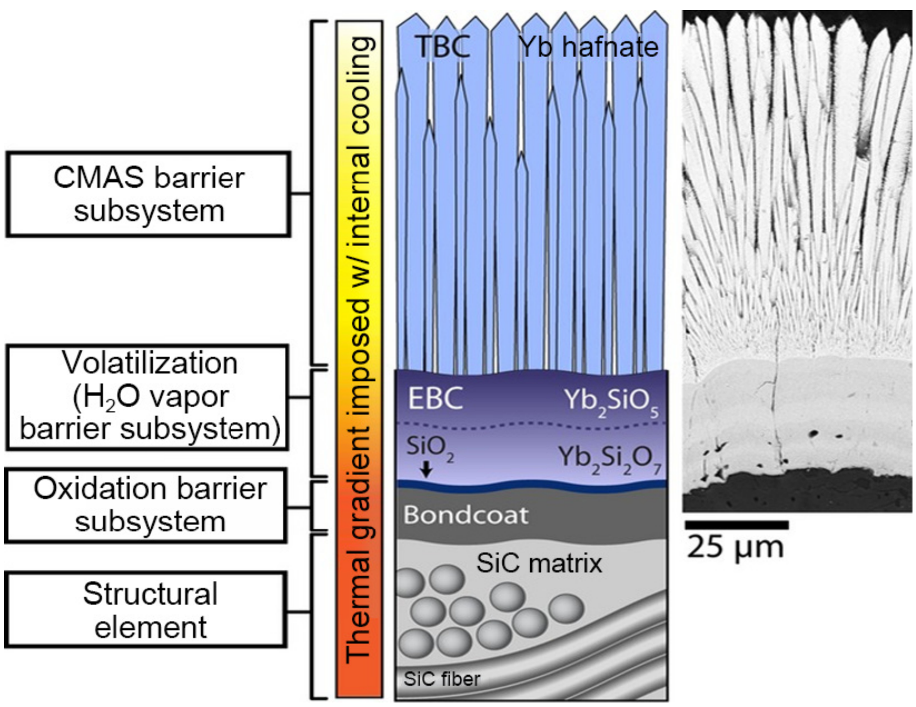

Fig. 2 Concept of new TBC/EBC composite coating system. Reproduced with permission from Ref. [12], © The American Ceramic Society 2014.

suitable material systems and design coating structures to improve the thermal insulation performance and corrosion resistance of coatings simultaneously [13].

The top coat of TBCs is mainly 7%–8% Y_2O_3 partially stabilized ZrO_2 (7–8YSZ), which has become the most widely used material of the top coat and has been the most mature material in the last five decades [23–26]. The tetragonal-monoclinic phase transformation above 1200 °C and CMAS corrosion limit YSZ application in advanced aeroengines where the maximum temperature exceeds 1600 °C [27,28]. At present, some researchers have attempted to improve the water vapor and CMAS corrosion resistance of zirconia-based TBCs to achieve some degrees of feature characteristics of EBCs [29,30]. Ball *et al.* [31] explored the effects of Er, Yb, Sm, and Gd rare earth elements as dopants for YSZ coatings and improved the CMAS resistance. The state-of-the-art of EBC ceramics and TBC ceramics has achieved low thermal conductivity and chemical reaction inertia without serious loss of other properties by applying high-entropy methodology, but their thermal cycling performance is not adequate because of a lack of understanding of the nonequilibrium thermal spraying process. In-depth analysis of the evolution of the microstructure, phase composition, and thermal-mechanical properties of feedstock powder for the coating preparation of TBCs and EBCs is essential for realizing integrated TBCs/EBCs in the future (Fig. 3).

Compared with single rare-earth component systems, multicomponent high-entropy systems can introduce more lattice distortions, high-entropy effects, hysteretic diffusion, and cocktail effects [32], resulting in higher hardness, lower thermal conductivity, and better corrosion resistance, which can result in a high-entropy ceramic layer with superior comprehensive performance at one time [33,34]. More noncorporate-funded research organizations are involved in TBC/EBC material research, but gradually, the physical properties of material and the feasibility of practical engineering applications have begun to develop independently, or even contrary. Through the recent 10 years of research on high-entropy ceramics, as shown in Fig. 4, laboratory researchers have focused on the physical and chemical properties of the material itself, but little research has been conducted on coating manipulation technology. The impacts of feedstock powder and thermal-spraying technology on the performance and thermal cycle lifetime of TBCs and EBCs are grossly underestimated because of the gap between demo theoretical studies and scale-up practical applications.

Few studies have shown that the elements, crystal phases, and melting states of high-entropy ceramic powder are significantly different from the design state because they undergo the nonequilibrium process of high-temperature spraying [32]. The physical and chemical properties out of the theoretical optimization ranges of the as-received coatings are unable to conform to the projected service lifetime and performance. Additionally, the amorphous phase is inevitable due to the rapid solidification of molten silicate during plasma spraying of rare-earth silicate coatings, which probably increases the risk of creep fatigue damage [35]. Yu *et al.* [36] reported that the $LaYbZr_2O_7$ coating and feedstock powder have different phase compositions. The feedstock powder consisted of both fluorite and pyrochlore phases. The coating prepared by atmospheric plasma spraying (APS) shows a new fluorite phase that is a thermodynamically nonequilibrium phase. Many studies have reported that the size of feedstock powder affects the phase compositions of thermally deposited rare earth disilicate EBCs [37,38]. Although adjusting the thermal spraying parameters (e.g., plasma arc current, gas flow rate, and hydrogen content) can be used to control the splat-like structure and properties of TBCs/EBCs, it is difficult to obtain a clear correlation between the spraying parameters and microstructure of the coatings because of the unstable inner structure and rough morphologies of the feedstock powder [39,40]. The melting status of feedstock powder during heating depends on their density, sphericity, inner structure, and size, which strongly affect the thermal-mechanical properties of the deposited coatings. To achieve precise control of the particle trajectories and temperature history, it is important to have a systematic understanding of the basic phenomena governing momentum, heat, and mass exchange between the plasma and the particles, as well as transient heat propagation into the particles [41–43]. Therefore, optimization of the feedstock powder could conveniently increase the overall uniformity and flowability of particles made of binary ceramics or multicomponent medium/high-entropy ceramics, which would greatly increase the manufacturing accuracy of thermally deposited coatings on both the composition and structural sides, eliminating component segregation and abnormal pore defects [44–46].

Recently, researchers at NASA [47], Max Planck Institute [48], Wuhan University of Technology [49], Shanghai Jiao Tong University [50], Xi'an Jiaotong University [51], Harbin Institute of Technology [52,53], and Beijing Institute of Technology [54,55] have investigated the effects of the nanoscale and hierarchical microstructures of feedstock powder made of YSZ, $La_2Zr_2O_7$, $LaMgAl_{11}O_{19}$, $Yb_2Si_2O_5$, and X2-Lu_2SiO_5 $(Sm_{0.2}Gd_{0.2}Dy_{0.2}Er_{0.2}Yb_{0.2})_2Zr_2O_7$ on the thermal conductivity and strain tolerance of deposited coatings. Guo's group [50,56,57] prepared electrostatic spraying associated with phase inversion technique (ESP)-YSZ microspheres with hierarchical inner structures that increased the 1100 °C thermal cycle lifetime of ESP-YSZ coatings by more than 3 times compared with that of coatings thermally deposited with commercial hollow spherical powder (HOSP).

Because feedstock powder is among the factors affecting the structure and properties of ceramic coatings, manipulation of both the configuration and structure of spraying powder on multicomponent medium/high-entropy ceramics in the context of advanced thermal spraying technologies is a promising path for

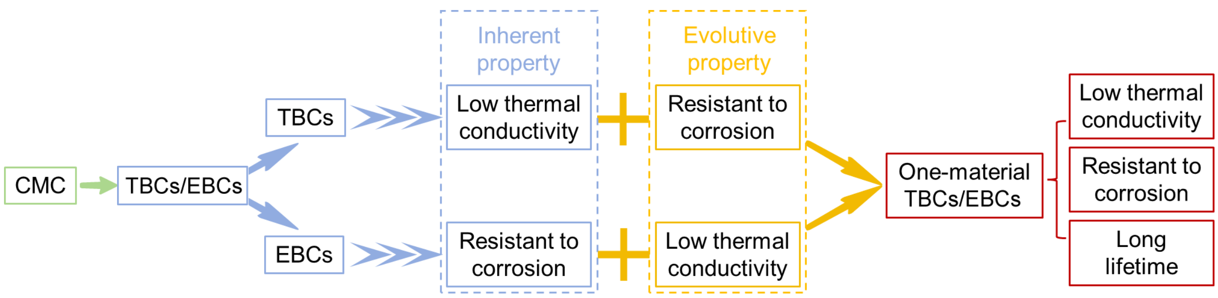

Fig. 3 Research and development path of TBCs/EBCs.

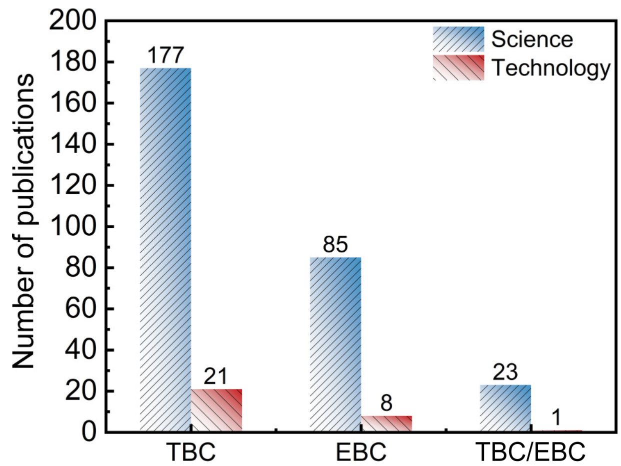

Fig. 4 Papers published on TBCs, EBCs, and TBCs/EBCs made of high-entropy ceramics in the past 10 years.

achieving high-performance TBCs/EBCs (Fig. 1(b)). Here, we reviewed the progress of medium/high-entropy ceramics, manufacturing technologies for feedstock powder, and relevant thermal-mechanical properties of ceramic coatings. In particular, the relationships among the morphology and microstructure of feedstock powder and the thermal conductivity, strain tolerance and phase composition of the as-received ceramic coatings were discussed thoroughly. This review aims to establish a link between material science and feedstock powder manipulation technologies on the basis of the current development of TBCs and EBCs, identifying blind spots on both sides and accelerating applications of long-lifetime TBCs/EBCs.

2 Granulation technology for ceramic powder

Altering the morphology and structure of ceramic powder can directly affect the structure of coatings, which in turn influences the properties of TBCs/EBCs [58]. The granulation technologies of feedstock powder mainly include traditional preparation techniques and techniques that can be used to prepare powder with refined structures. The following is a systematic introduction to these methods and their application progress.

2.1 Traditional granulation technology of feedstock powder

The traditional preparation techniques for feedstock powder include the sol–gel method [59], high-temperature melting method [60], templating method [61,62], spray drying method [63], etc. Figure 5 shows the various shapes of spraying feedstock powder produced via different traditional preparation techniques [64]. Although the feedstock powder melt into spheres during

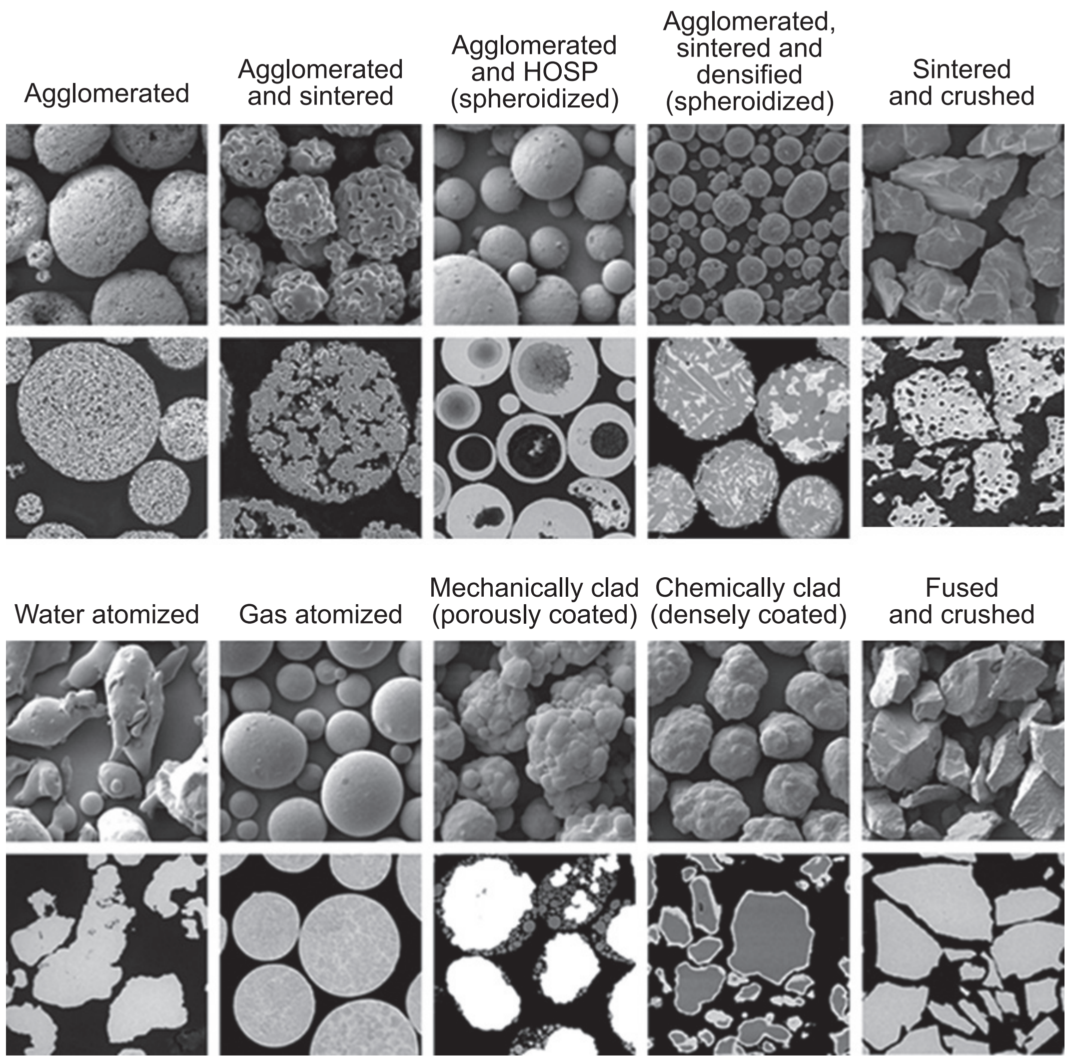

Fig. 5 Traditional feedstock powder morphologies. Reproduced with permission from Ref. [64], © American Institute of Chemical Engineers 2019.

deposition, the initial morphology and pore structure of the feedstock powder are important parameters in the spraying process. Even if the feedstock powder exhibits the same particle size distribution and chemical composition, the difference in initial structure and morphology also leads to significant differences in coating structure and properties.

The production efficiency of most techniques is relatively low, and these techniques are only suitable for the laboratory. Only high-temperature melting and spray-drying methods can be applied to large-scale production. The high-temperature melting method transports powder into a flame and melts them to form dispersed microdroplets, which solidify into microspheres through the cooling zone [23]. The high-temperature melting method can adapt the melting temperature, holding time, and ratio of feedstock powder according to the actual needs to control the size, shape, and structure of microspheres, which is usually suitable for the preparation of high-temperature stable microspheres, such as alumina microspheres. As the ceramic powder is completely molten into the liquid during the melting process and exhibits excellent flowability, the sphericity of the microspheres after cooling and solidification is high, and the surface of the microspheres is smooth. However, owing to the difficulty in controlling the cooling process, the wall thickness of hollow ceramic microspheres is not uniform. In addition, the microspheres may undergo a phase transition during the high-temperature melting process, which impacts the coating properties. The preparation of ceramic microspheres via the spray drying method is a process in which the atomized droplets are rapidly solidified into microspheres via a drying medium [65,66]. During spray drying, the morphology and structure of the microspheres can be controlled by adjusting the parameters of the sprayer (nozzle diameter, pressure, spray angle, etc.), temperature, humidity of the dryer, and other parameters. In addition, adding surfactants and adjusting the concentration of the solution also affect the morphology and size of the powder [46].

Spray drying is the most commonly used granulating technology for preparing TBCs/EBCs. The sizes of ceramic powder prepared by spray drying are typically from 1 to 100 μm, with relatively high dispersion, and usually present hollow or porous structures, which mainly depend on the evaporation rate of the solvent during the drying process as well as the material characteristics. The solvent typically evaporates from the surface of powder during the drying process, forming a hollow structure. However, the porous structure tends to form inside powder when the evaporation rate of the solvent is slow. Moreover, the process stability of spray drying is poor because of the limited preparation parameters, and it is impossible to accurately control the internal structure of powder [23,66]. Zhu *et al.* [67] prepared $Gd_2Zr_2O_7$ feedstock powder via spray drying, which exhibits greater sphericity and hollow structures than commercial powders do. However, because the slurry is affected by hot air in the dryer, the surface of the spray-dried powder inevitably has a rough morphology, which affects the sphericity and flowability of the powder. Feedstock powder with low sphericity and poor flowability often lead to problems such as component segregation in coatings. Additionally, the amorphous phase is inevitable because of the rapid solidification of molten silicate and volatilization of Si during plasma spraying of rare-earth silicate coatings after spray drying. The loss of Si can be reduced by adjusting the spraying parameters to control the stoichiometric ratio and phase content. In addition, the microcracks and porosity of the coating can also be effectively controlled [39,40].

The heat and momentum transfer between powder and plasma jets are affected by the sphericity, density, structure, and size distribution of spraying powder, leading to differences in the melting state and velocity when powder stacks to form a splat-based coating [41–43]. Therefore, adjusting the structure of feedstock powder for a more uniform composition distribution and better flowability can help the powder be more evenly distributed, reducing the degree of component segregation caused by the difference in the diffusion rates of different components during deposition [44]. Moreover, the cooling rate and other parameters during melting and solidification can be controlled by adjusting the structure and morphology of feedstock powder, which is conducive to forming a more stable crystal structure and reducing the appearance of metastable crystals. Li *et al.* [52] conducted plasma treatment on $Yb_2Si_2O_7$ powder after spray drying. The $Yb_2Si_2O_7$ powder has good density and sphericity and has a smooth surface, as shown in Fig. 6. The flowability can reach 136.4 $g\cdot min^{-1}$, which is much higher than that of the powder before plasma treatment (56.65 $g\cdot min^{-1}$). Additionally, the particle size of the $Yb_2Si_2O_7$ powder after plasma treatment is distributed between 10–53 μm, which is suitable for APS. Guo *et al.* [55] improved the spray drying method and adopted the nanopowder reconstitution method, which consists of three steps—wet ball-milling, spray granulation, and high-temperature sintering—to successfully prepare nanostructured X2-Lu_2SiO_5 feedstock powder with a single phase. The feedstock powder exhibits good flowability, and the internal structure is relatively dense, which can effectively improve the density and wear resistance of the coatings.

2.2 Microfluidic techniques

Microfluidic techniques can control microdroplets via microflow channels and microflow control devices (Fig. 7) [68]. These techniques are often appropriate for preparing micron-sized microspheres with specific functions and complex structures because of their precise controllability at the microscale. Liang *et al.* [69] prepared ZrO_2 microspheres from $ZrOCl_2 \leftrightarrow H_2O$ by exploiting microfluidics. The microspheres exhibit high sphericity and can be precisely controlled in the size range of 20–200 μm.

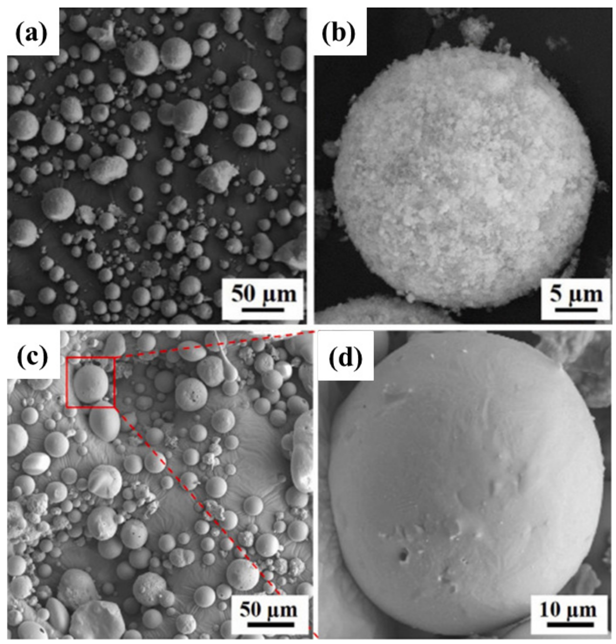

Fig. 6 (a, b) Morphologies of powder after spray drying. (c, d) Morphologies of powder after plasma treatment. Reproduced with permission from Ref. [52], © Elsevier Ltd and Techna Group S.r.l. 2023.

Chu *et al.* [70] utilized three-stage capillary glass microfluidics to prepare microspheres with hierarchical structures, further validating the great potential of microfluidics in the control and preparation of complex ceramic microsphere structures. However, the application range of this technology is currently limited, and it still faces difficulties, including complex processes and long periods, making it challenging to precisely control the ceramic powder structure at the microscale.

To address the shortcomings of current microfluidic techniques, Guo *et al.* [50] invented a method for the preparation of thermally sprayed microspheres via electrostatic spraying associated with the phase inversion technique (ESP), which combines both electrostatic spraying and phase inversion to overcome the limitations of structural control in traditional methods, as shown in Fig. 8 [71]. In the electrostatic spraying process, a voltage is applied between the nozzle and the

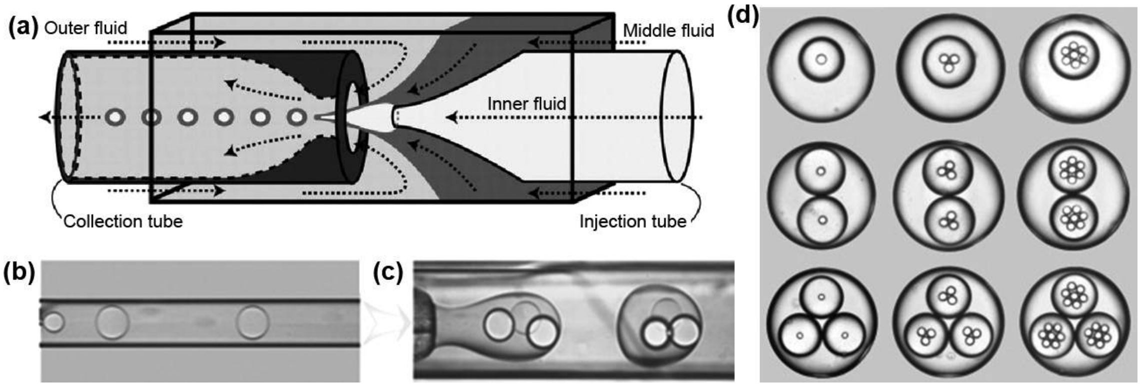

Fig. 7 (a) Schematic diagram of a microfluidic device, (b, c) morphologies of microdroplets at different stages, (d) microdroplets with different internal structures. Reproduced with permission from Ref. [70], © WILEY-VCH Verlag GmbH & Co. KGaA, Weinheim 2007.

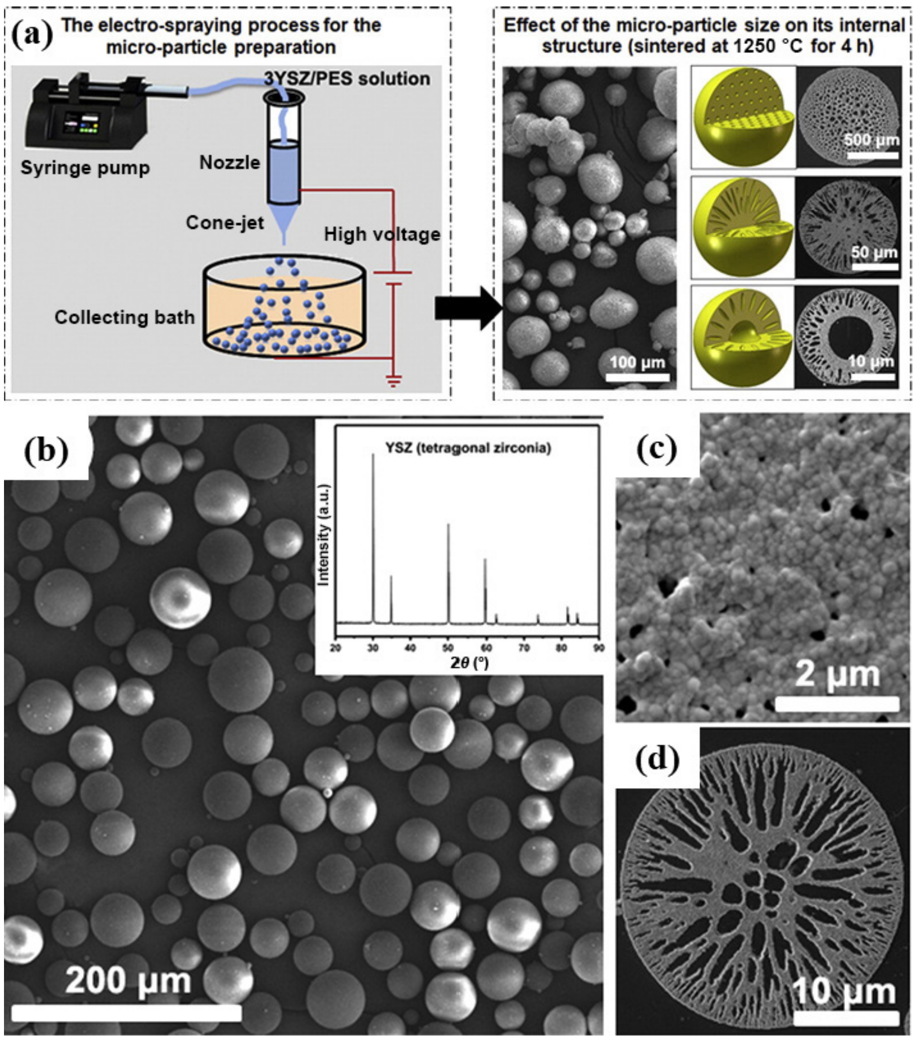

Fig. 8 (a) Schematic diagram of ceramic microspheres prepared via ESP, (b) surface morphology, (c) outer surface, and (d) polished cross section of ESP-YSZ microspheres. Reproduced with permission from Ref. [50], © Elsevier Ltd 2017.

coagulation bath. The droplets are dispersed into tiny droplets under the action of an electric field. The insoluble organic matter in the coagulation bath is deposited with ceramic powder in the solid phase and forms different pore structures through phase inversion. Finally, the organic matter is removed by sintering at high temperatures to obtain ceramic microspheres. The structure of microspheres prepared via ESP can be divided into three parts: epidermis, finger-like pore structure, and sponge-like structure, as shown in Fig. 5(d). Moreover, micrometres and nanometers are simultaneously two different pore structure sizes in microspheres [56].

In addition, the ESP technique can control the size, structure, morphology, and properties of microspheres by adjusting the electrospray parameters and sintering temperatures [50]. Guo *et al*. [50] investigated the effect of voltage on the particle diameter of ESP microspheres, and the results showed that the particle diameter decreases with increasing voltage and that the particle diameter could be constantly changed in the range from 100 to 1000 μm by adapting the voltage. When the voltage is low, the electrostatic pressure of the liquid makes it difficult to overcome the surface tension, causing the slurry to form millimeter droplets under gravity. When the voltage exceeds the critical value, the electrostatic force can overcome the surface tension, making the droplets unstable and finally decomposing into microdroplets. Zhang *et al*. [72] used ESP microspheres to prepare ZrB_2(Z)–20 vol% SiC(S) spiral fibers (ZS_{sf}) and investigated the effects of phase inversion process parameters on the internal microstructures of ESP microspheres. The results showed that the nonequilibrium phase transition is prone to form a finger-like pore structure, whereas the dense structure is conducive to forming during delayed phase transition, as shown in Fig. 9. The macroscopic structure of ESP microspheres is almost unaffected by the sintering temperature. However, as the sintering temperature increased, the porosity of the ESP microspheres tended to decrease, and the sponge-like structure tended to be denser while the micropores gradually disappeared [56].

Xing *et al*. [56] compared the heat transfer and mechanical properties of YSZ-ESP microspheres and YSZ-HOSP and reported that the thermal conductivity of ESP microspheres is 30%–40% lower than that of HOSP powder, which is attributed to the synergistic resistance effect of the hierarchical pore structure on heat transfer. Microfinger-like pores inhibit heat transfer and are thus difficult to sinter, as nanopores can increase phonon scattering [57]. A support structure composed of finger-like pores is beneficial for improving the mechanical properties of microspheres with hierarchical porous structures. According to the numerical simulation results of the ESP microsphere uniaxial compression shown in Fig. 10, the finger-like pore wall stress perpendicular to the pressure direction is the highest in the compression process. The pore structures inside the microspheres caused multiple deflections of crack growth, which could increase the crushing energy of the microspheres. Therefore, the compressive strength and crushing energy absorption capacity of the ESP microspheres are both greater than those of the HOSP powder at the same porosity.

Yu *et al*. [57,73] prepared lanthanum zirconate ($La_2Zr_2O_7$, LZO) microspheres via ESP and estimated the thermal conductivity of LZO microspheres via a novel nest model derived from the Maxwell–Eucken model and the EMT model. The hierarchical pore structure can induce heat deflection and inhibit

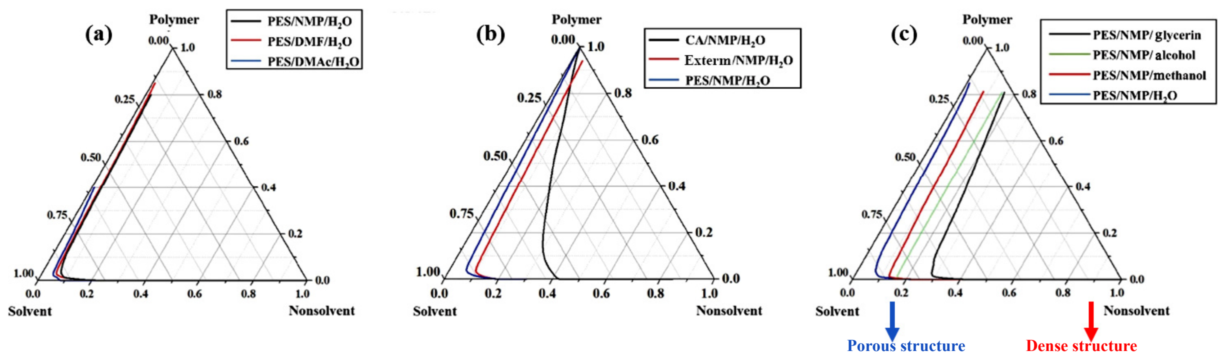

Fig. 9 Effect of phase inversion process parameters on internal microstructure of ZS_{sf}. Reproduced with permission from Ref. [72], © The Author(s) 2022.

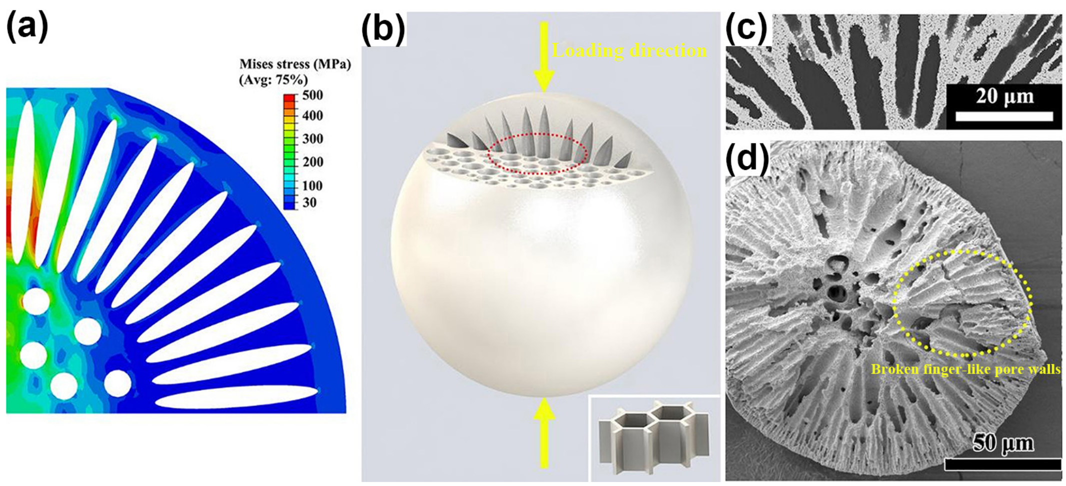

Fig. 10 (a) Stress distribution of ESP microspheres, (b) schematic diagram of three-dimensional structure of ESP microspheres, (c) finger-like pore wall, and (d) fracture morphology of ESP microspheres. Reproduced with permission from Ref. [56], © Elsevier Ltd and Techna Group S.r.l. 2021.

heat transfer from the surface to the interior of the microspheres, resulting in an approximately 20% lower thermal conductivity for the LZO-ESP microspheres than for the LZO-HOSP microspheres, which have similar porosities. Briefly, the heat flow distribution curve inside the ESP microsphere is more tortuous, which can effectively prolong the heat flow distribution path, resulting in increased scattering and thermal resistance (Fig. 11). The effect of granulation technology on the structure and properties of feedstock powder is highly significant. Even with the same granulation technology, different granulation parameters may lead to differences in the internal structure, external morphology, sphericity, and particle size distribution of feedstock powder, affecting the properties of feedstock powder and leading to different structures and properties of the deposited coatings. Different sintering temperatures of the microsphere precursor usually cause the $(Sm_{0.2}Gd_{0.2}Dy_{0.2}Er_{0.2}Yb_{0.2})_2Zr_2O_7$-ESP-microspheres to have various internal structures [74]. After sintering at 1000 and 1200 °C, many intergranular pores exist in the sponge-like structural region of the ESP microspheres. As the sintering temperature increased to 1550 °C, the intergranular pores gradually healed, and only some large pores remained in the microspheres, as shown in Fig. 12. Moreover, with increasing

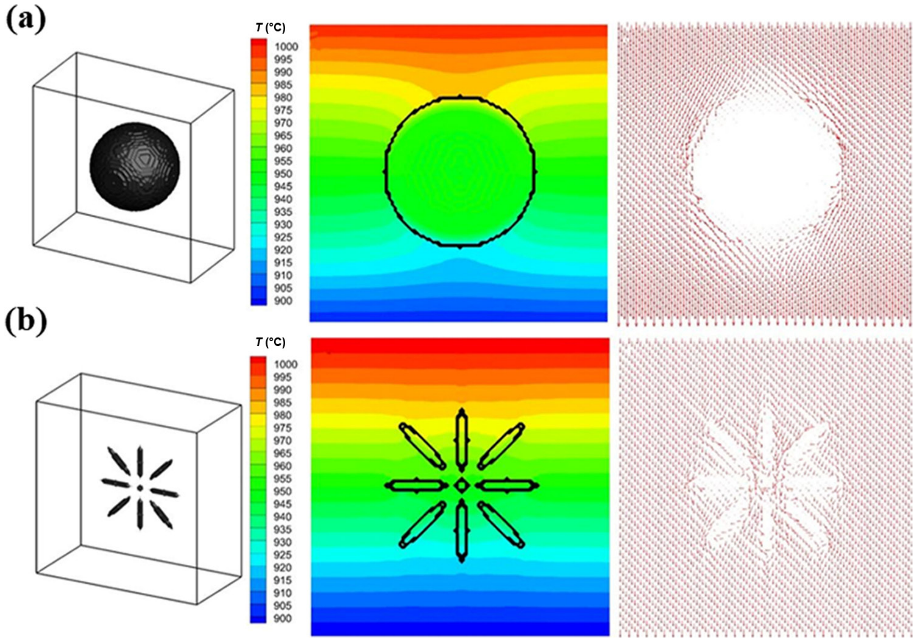

Fig. 11 Effect of (a) HOSP microsphere structure and (b) ESP microsphere structure on temperature and heat flow distributions. Reproduced with permission from Ref. [57], © The Society of Powder Technology Japan 2022.

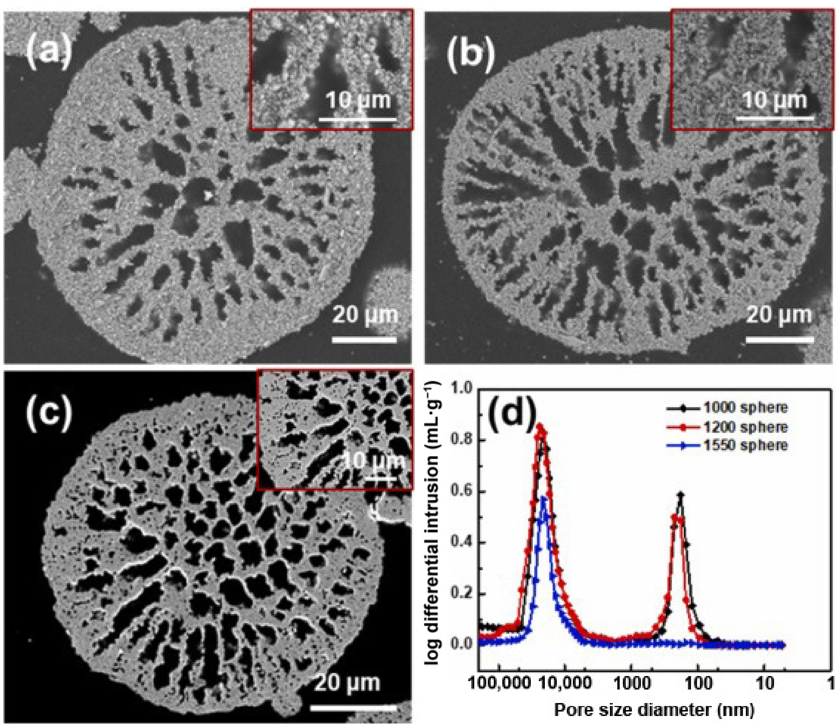

Fig. 12 Cross-sectional images of ESP microspheres sintered for 2 h at (a) 1000 °C, (b) 1200 °C, and (c) 1550 °C, and (d) the pore size distribution inside ESP microspheres. Reproduced with permission from Ref. [74], © Elsevier Ltd. 2024.

sintering temperature, the thermal conductivity and compressive strength of single microspheres increase. The microsphere sintered at 1550 °C has the highest thermal conductivity (0.64 W·m⁻¹·K⁻¹), which is one third of that of the dense $(Sm_{0.2}Gd_{0.2}Dy_{0.2}Er_{0.2}Yb_{0.2})_2Zr_2O_7$ ceramics (1.85 W·m⁻¹·K⁻¹).

3 Structural, thermal, and mechanical properties of thermally sprayed ceramic coatings

3.1 Effects of monotonical pore structure on coating properties

The service lifetime and heat insulation of TBCs/EBCs are influenced by the microstructure of feedstock powder in addition to the process parameters during thermal spraying [75,76]. The structure and properties of powder affect their molten state in the plasma flame, which in turn affects the structure and properties of TBCs/EBCs [75,77,78]. The traditional powder used for thermal spraying can be divided into HOSPs, agglomerated and sintering powder (A&S), and fused and crushed powder (F&C). F&C powder is dense, and the coating prepared from F&C powder has the highest density and high thermal conductivity among them. Moreover, owing to the faster sintering rate of the dense coating, the F&C coating manifests a high elastic modulus.

In contrast, the loose structure of coatings prepared from porous powder, such as HOSP and A&S powder, can effectively reduce the densification of the coatings, resulting in a low elastic modulus (Fig. 13) [71]. A&S powder is composed of multiple micron particles, and the surface is relatively rough. Compared with those of A&S powder, the surfaces of HOSP powder are smoother, but there are still noticeable defects and pores, and the whole sample appears as a hollow sphere with a thin and dense shell. The deposition efficiency of the A&S powder is greater than that of the F&C powder at the same density, and the thermal conductivity of the A&S coating is lower than that of the F&C coating because of the high interlayer porosity of the A&S coating. HOSP powder is more prone to form thin lamellas than A&S powder is, resulting in higher porosity and interlayer porosity. Consequently, the thermal conductivity of the HOSP coating is lower than that of the A&S coating [76–78].

Allen *et al.* [76] compared the structures of F&C coatings and HOSP coatings and reported that the two coatings had significantly different cross-sectional structures. The F&C coating retains part of the lamellar structure, whereas the HOSP coating almost completely loses the lamellar structure. Dwivedi *et al.* [79] used F&C and HOSP powder to prepare YSZ coatings by APS under the same spraying process and discovered that the density of the F&C coating was greater than that of the HOSP coating, leading to a greater elastic modulus and fracture toughness of the F&C coating. Because of its higher density during the sintering process at 1200 °C, the F&C coating is sintered more quickly than the HOSP coating is. Tan *et al.* [80] also compared the properties of F&C coatings and HOSP coatings and reported that the porosity of F&C coatings is lower than that of HOSP coatings. Because the HOSP coating has thinner lamellae and more pores, which effectively enhances phonon scattering, the thermal conductivity of the F&C coating is higher than that of the HOSP coating by approximately 0.2 W·m⁻¹·K⁻¹. Ercan *et al.* [81] prepared coatings exploiting HOSP and A&S powder. The thermal conductivities of these two coatings are similar. However, the glass phase in the A&S powder accelerated the slip of the grain boundaries, facilitating coating densification and resulting in higher thermal conductivity in the A&S coating than in the HOSP coating after being sintered at 1400 °C for 50 h. Additionally, many spherical pores originating from the HOSP powder were retained in the HOSP coating and did not disappear after sintering. Kulkarni *et al.* [75] prepared three kinds of TBCs employing F&C powder, A&S powder, and HOSP powder. A comparison of the heat insulation and mechanical properties of these three kinds of coatings revealed that the F&C and HOSP coatings presented obvious lamellar structures, indicating a significant difference between the elastic moduli of these two coatings in the surface and cross-sectional directions, with a higher elastic modulus in the surface direction. However, A&S coatings have similar elastic moduli in the surface and cross-sectional directions because A&S coatings lack an obvious lamellar structure. Ilavsky *et al.* [82] employed the neutron diffraction method to show that powder with the same composition but different morphologies has different phase compositions after plasma spraying.

The coatings prepared by plasma spray-physical vapor deposition (PS-PVD) exhibit a similar service lifetime as EB-PVD and a similar thermal conductivity as APS (Fig. 14) because of the structure of the PS-PVD coatings. Compared with EB-PVD coatings, such coatings are composed of feather-like structures and display more complex secondary, tertiary, or even multilevel branch structures on the main body columnar structure, generating abundant complex dendrite pores and hindering heat transfer [83]. Moreover, the complex feather-like structure can provide more paths and spaces, making it difficult for CMAS to form a continuous infiltration path. CMAS corrosion and water vapor corrosion lead to a reduction in both the durability and reliability of TBCs/EBCs [84–89]. However, CMAS corrosion is generally the main cause of TBC/EBC failure when the engine operating temperature exceeds 1200 °C [90–92]. Wang *et al.* [93] prepared two YSZ coatings by using APS and PS-PVD and carried out static corrosion experiments at high temperatures. The results revealed that the laminar coatings prepared by APS experienced overall spalling in a short time, whereas the feather-like coatings prepared by PS-PVD experienced no significant

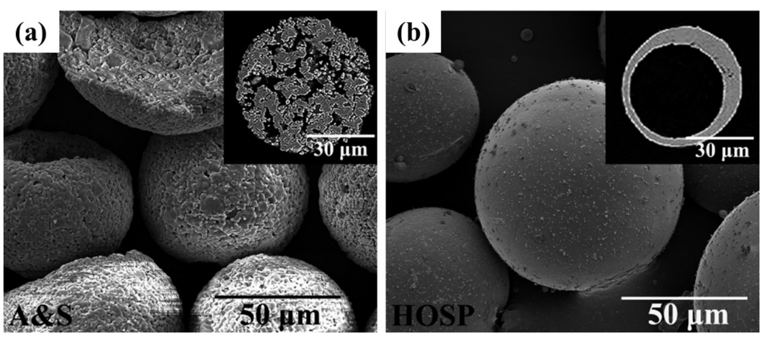

Fig. 13 Morphologies of commercial YSZ powder: (a) A&S and (b) HOSP. Reproduced with permission from Ref. [71], © The American Ceramic Society 2018.

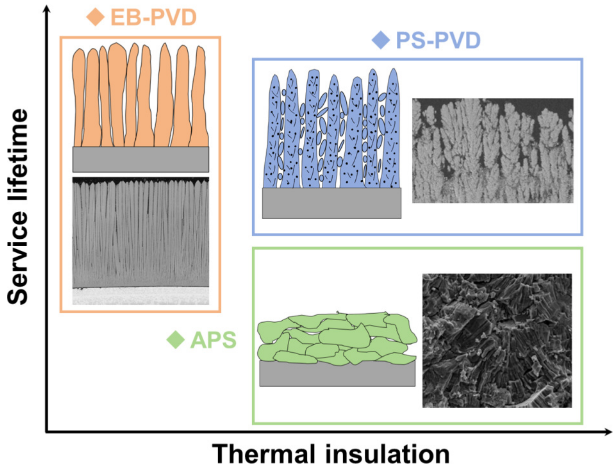

Fig. 14 Comparison of microstructures, thermal insulations, and service lifetimes of TBCs prepared with APS, EB-PVD, and PS-PVD. Reproduced with permission from Ref. [22], © Elsevier 2019; Ref. [71], © The American Ceramic Society 2018; Ref. [94], © Elsevier Ltd. 2024; Ref. [95], © The Author(s) 2022.

spalling even after 20 h of CMAS corrosion, indicating that the resistance of the PS-PVD coatings to CMAS corrosion is greater than that of the APS coatings.

The phase state of the deposition unit can be modified by varying the particle size of the powder, feed rate, spraying distance, atmosphere composition, and other parameters to achieve gas–liquid, solid–liquid, or multiphase mixed deposition in the process of preparing coatings via PS-PVD to adjust the microstructure of the coatings and improve their properties [96,97]. Jia *et al.* [98] prepared YSZ powder with different structures via the spray-drying method and subsequently fabricated ceramic layers via PS-PVD to investigate the impact of powder features on the microstructure and deposition rate of the coating. Consequently, the powder could only be efficiently gasified in a plasma jet at a suitable particle size. In addition, "secondary agglomerates" are more favorable than "primary agglomerates" for forming coatings with columnar crystal structures and high deposition rates. Yin *et al.* [99] utilized PS-PVD to deposit YSZ powder with different original grain sizes and agglomeration particle sizes into columnar TBCs and explored the effect of powder on the structure and properties of TBCs (Fig. 10). The results illustrated that the gasification efficiency increases with increasing original grain size. Furthermore, as the particle size of the agglomerated powder increases, the roughness and porosity of the coatings tend to increase, increasing the deposition efficiency and thermal shock resistance but decreasing the bonding strength. The microstructure of a coating mainly depends on whether the powder can be effectively gasified at a suitable spraying distance, where the degree of powder gasification in a plasma jet is closely related to the spraying process, characteristics of the plasma jet, and the powder itself. Currently, the use of powder with controllable structures is the primary method used to regulate and control the microstructure and properties of coatings, providing high efficiency and convenient operation [41]. Although coatings prepared with PS-PVD have great advantages in terms of resistance to CMAS corrosion and low thermal conductivity, this technique has strict requirements for the structure and morphology of powder. Therefore, designing a kind of feedstock powder suitable for PS-PVD is urgent.

3.2 Effects of the bimodal pore structure on the coating properties

Many studies have been devoted to the preparation of TBCs by using nanostructured feedstock powder in recent years. The microstructure and morphology of ceramic microspheres prepared by ESP differ from those of traditional feedstock powder, resulting in differences in the properties of powder. ESP provides a new technique for preparing ceramic microspheres and realizing the precise manipulation of the structure and morphology of ceramic powder to confer hierarchical pore structures [100]. In contrast to TBCs made with traditional powder, nanostructured TBCs contain a dense region formed by the complete melting of powder while retaining loose and porous nanostructures due to incomplete molten powder [101]. Dense and nanostructured regions are stacked on each other to form nanostructured TBCs, also known as bimodal TBCs [101–103]. Nanomaterial are characterized by quantum size effects, small size effects, interface and surface effects, etc. Compared with traditional ceramics, nanomaterial exhibit excellent plasticity and ductility due to their abundant interfaces [104,105]. Nanostructured TBCs exhibit obvious advantages in terms of high-temperature mechanical properties and thermal insulation. Moreover, the nanoregions of nanostructured TBCs can control crack extension, which can improve the bonding properties between lamellae and increase the thermal cycle lifetime [106,107], as confirmed by Liang and Ding (Fig. 15) [108]. This is primarily due to the high porosity of nanostructured TBCs, which can not only slow the densification of coatings and increase the strain tolerance of the coating but also reduce the thermal conductivity and improve heat insulation. Moreover, the "bistate effect" and "pinning effect" of nanostructured TBCs can hinder grain growth and result in excellent phase stability at high temperatures [109].

Owing to the excellent thermal and mechanical properties of nanostructured TBCs, retaining part of the pore structure can not only reduce the thermal conductivity by increasing phonon scattering but also improve the strain tolerance of coatings by toughening micropores. Zou *et al.* [71] prepared three kinds of TBCs by APS with the same spraying parameters as the ESP, A&S and HOSP powder (Fig. 16). A comparison of the morphologies and structures of these three kinds of TBCs revealed that the ceramic layers prepared with the A&S and HOSP powder were composed of completely molten powder, where the present columnar crystals were lamellar. However, there are not only completely molten regions in the ceramic layers prepared with ESP powder but also semimolten regions or even regions that still maintain the original morphology of the powder (Figs. 16(f) and

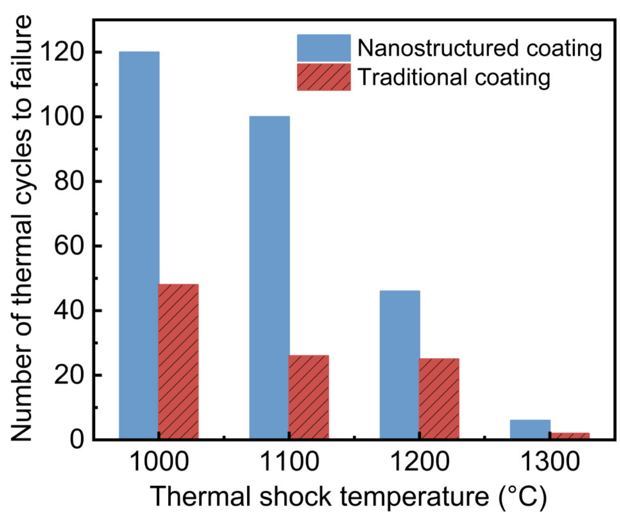

Fig. 15 Thermal shock resistance of nanostructured TBCs and traditional TBCs. Reproduced with permission from Ref. [108], © Elsevier B.V. 2004.

16(i)). The proportion of incompletely molten regions can reach 20%. A comparison of the porosities of these three coatings revealed that the ceramic layer prepared with the ESP powder has the highest total porosity (Fig. 16(j)), mainly because of the large number of loose porous regions. The ceramic layer prepared with the A&S powder has the highest content of spherical pores, whereas the ceramic layer prepared with the ESP powder has the highest content of microcracks and tine pores. In addition, the thermal cycle lifetime of the ceramic layer prepared with ESP powder is 2–3 times longer than that of the other two ceramic layers.

Xing *et al.* [110] used ESP and HOSP powder to prepare TBCs by employing APS and compared the structures and properties of the coatings. Compared with the HOSP coating, the ESP coating not only has extremely low initial thermal conductivity (0.70 $W·m^{-1}·K^{-1}$), approximately 50% of the thermal conductivity of the HOSP coating but also has superior phase stability and heat insulation at high temperatures. The thermal conductivity of the ESP coating only increased to 1.29 $W·m^{-1}·K^{-1}$ after being sintered at 1400 °C for 128 h, as shown in Figs. 17(a)–17(d). The ESP coating is distributed in two regions with different structures. One is a loose porous region with dark contrast, and the other is a dense region of columnar crystals with bright contrast, belonging to the nanostructured TBCs, as shown in Figs. 17(e) and 17(f). Unlike the ESP coating, the HOSP coating presents a lamellar structure, with interlayer cracks as well as spherical macropores between lamellae, where no loose porous regions exist, as shown in Figs. 17(g) and 17(h). The differences in pore distribution and microstructure between the ESP coating and HOSP coating can cause different densification behaviors, resulting in separation and interlayer cracks between dense and unfused lamellas and the inhibition of heat flow transfer (Figs. 17(i) and 17(j)).

The excellent fracture toughness and anti-sintering ability can effectively delay the cracking and performance deterioration of the ESP coating, thus resulting in a good thermal cycle lifetime and thermal shock resistance. The content of partially molten powder in a coating can significantly affect the thermal cycle lifetime of the coating. As shown in Fig. 18(a), the thermal cycle lifetime of the ESP coating is 2–3 times longer than that of the HOSP coating. The crack growth tends to occur in the dense region, whereas the unmolten region inhibits it. The residual stress of the ESP coating is concentrated only in the indentation region. Moreover, the number of cracks caused by indentation is significantly lower than that caused by the HOSP coating under the same indentation

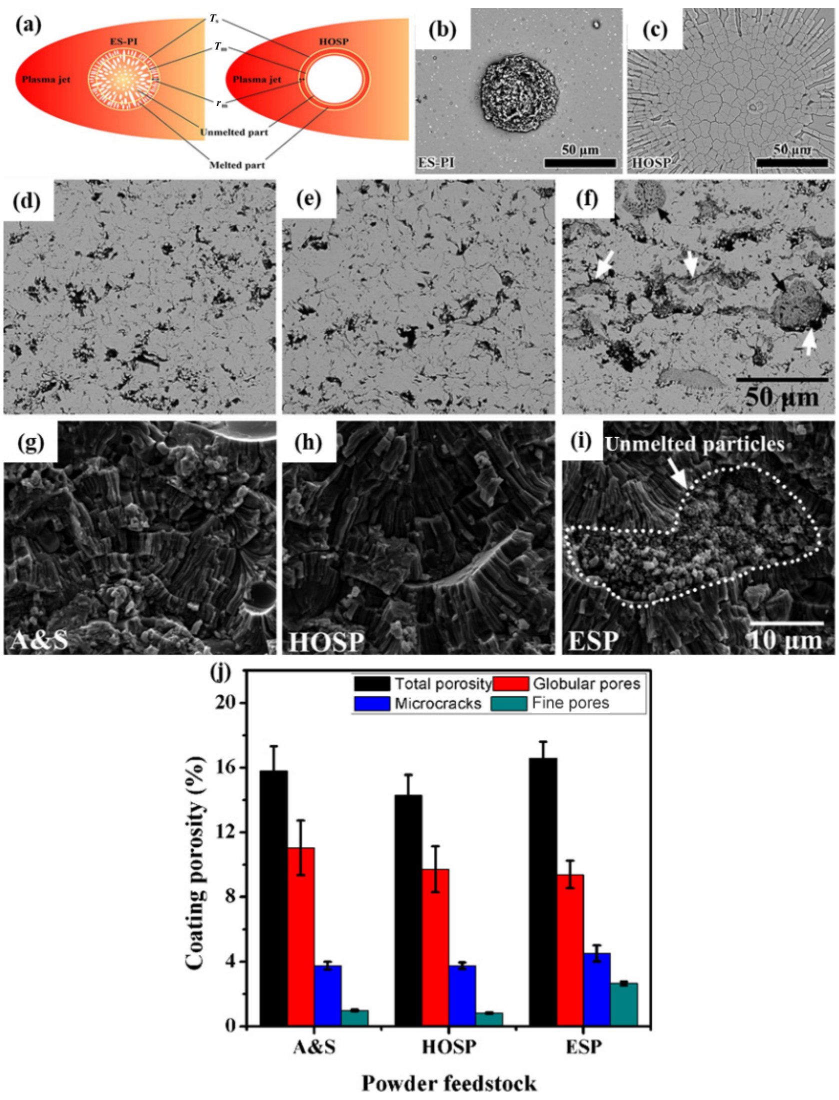

Fig. 16 (a) Schematic diagram of melting state; melting state of (b) ESP powders and (c) HOSP powders; microstructures of YSZ top ceramic layers deposited by (d, g) A&S, (e, h) HOSP, and (f, i) ESP powders; (j) porosity of YSZ ceramic top coats deposited by different powders. Reproduced with permission from Ref. [71], © The American Ceramic Society 2018.

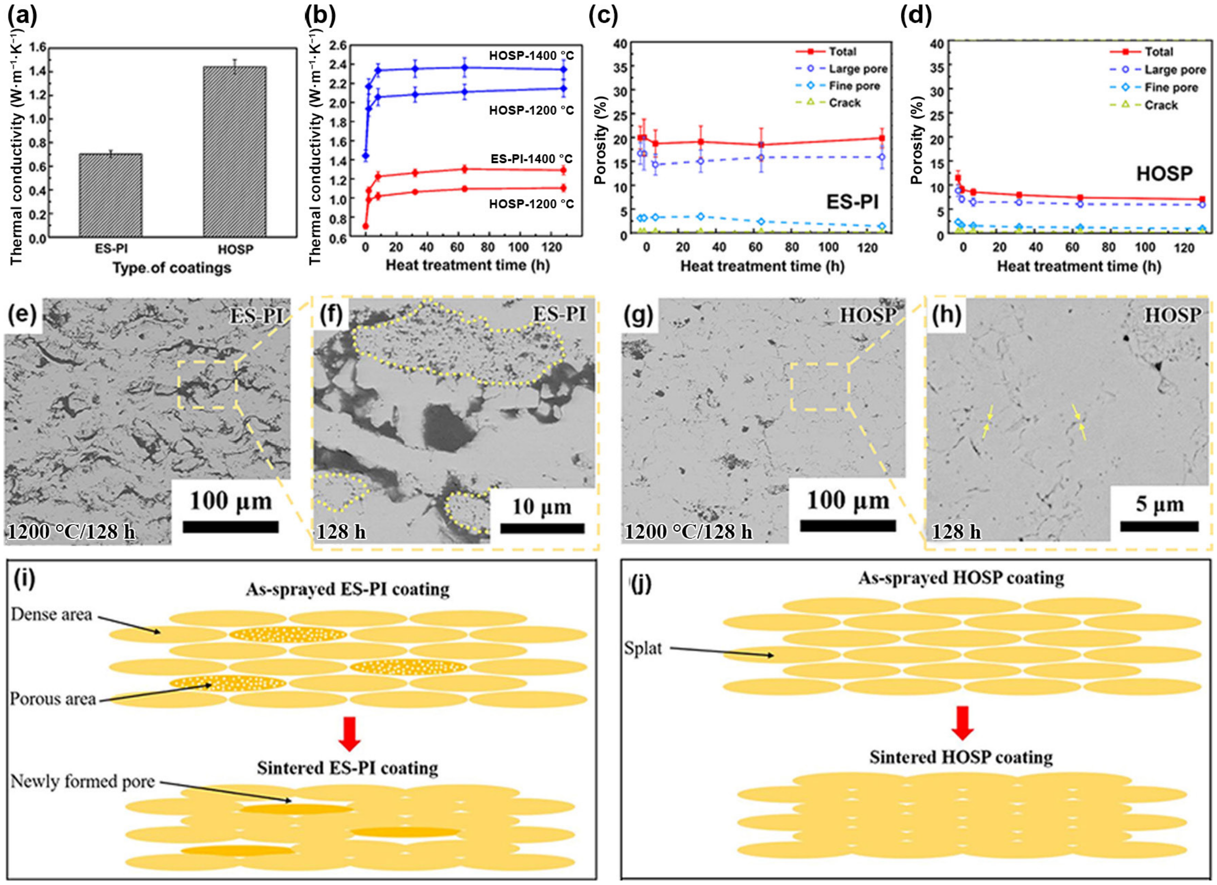

Fig. 17 Thermal conductivities and sintering behavior of ESP coating and HOSP coating: (a) thermal conductivity at room temperature, (b) thermal conductivity after isothermal treatment, and variation trend of porosity in (c) ESP coating and (d) HOSP coating with isothermal heat treatment. Morphologies of (e, f) ESP coating and (g, h) HOSP coating after isothermal heat treatment; Anti-sintering behavior diagram of (i) ESP coating and (j) HOSP coating. Reproduced with permission from Ref. [110], © The American Ceramic Society 2020.

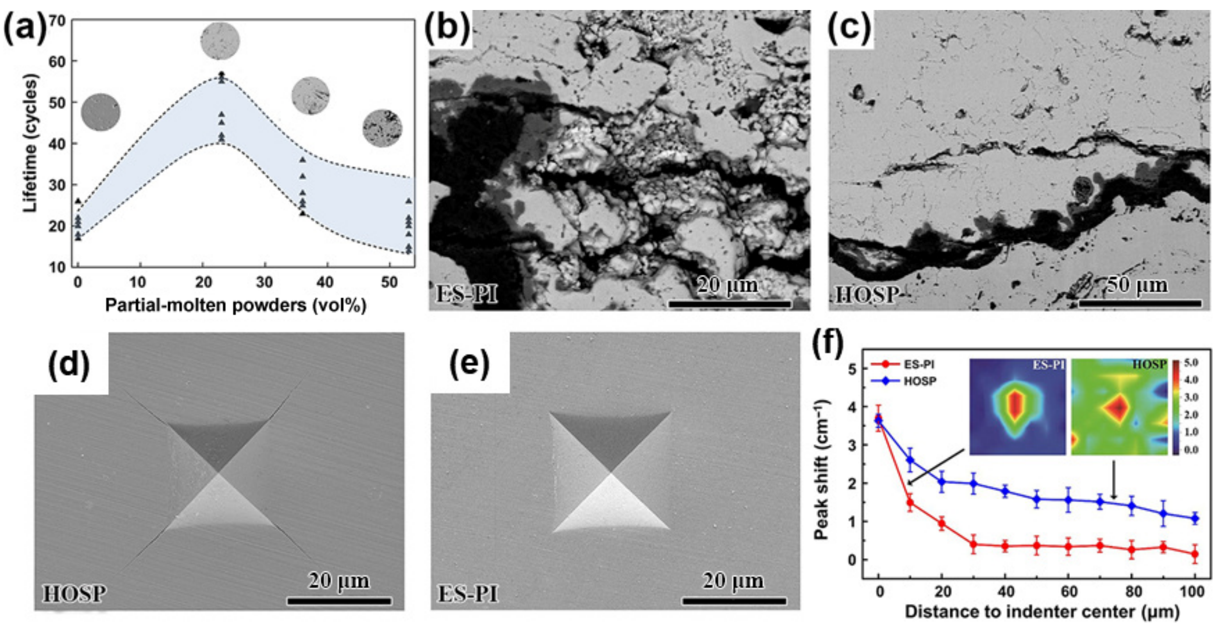

Fig. 18 (a) Thermal cycle lifetimes of ESP coating and HOSP coating and crack growth morphologies of (b) ESP coating and (c) HOSP coating after thermal cycling. Indentation stress fields of (d) HOSP block material and (e) ESP block material, and (f) Raman peak shifts in ESP and HOSP coatings and surrounding areas. Reproduced with permission from Ref. [100], © Elsevier Ltd. 2021.

stress field, indicating that the ESP coating has greater strain tolerance and a longer thermal cycle lifetime [100].

Zhou *et al.* [111] prepared $La_2(Zr_{0.75}Ce_{0.25})_2O_7$ (LCZ) powder by combining chemical coprecipitation and spray drying and prepared $La_2(Zr_{0.75}Ce_{0.25})_2O_7$ nanostructured TBCs via APS. The findings demonstrated that the coatings contain unmolten nanostructured regions and exhibit a typical bistate structure. Subsequently, Yang *et al.* [112] successfully prepared nanostructured LCZ ceramic coatings by applying LCZ nanopowder with a particle size of approximately 40 μm and compared the structure and properties with those of ceramic blocks made of LCZ nanopowder. The phase of the LCZ ceramic blocks is consistent with that of the LCZ nanopowder with a pyrochlore structure, whereas the LCZ coating presents a nonequilibrium fluorite phase. The thermal conductivity of the LCZ ceramics is 0.65 W·m⁻¹·K⁻¹, which is approximately 1/3 that of YSZ, and the CTE is 10.7×10^{-6} K⁻¹. Moreover, it shows good sintering resistance at 1500 °C for a long time (≥ 40 h), making it the ideal choice for TBCs. In addition, the size of the pores affects the thermal conductivity of coatings [113,114], in which nano- and submicron-sized pores have a greater influence on heat insulation. Thus, increasing nanopores by adjusting the structure of feedstock powder and process parameters can effectively improve the thermal protection of TBCs [75]. Yu *et al.* [36] explored the effects of the size of feedstock powder on the microstructure and thermal conductivity of $LaYbZr_2O_7$ TBCs. The results showed that the coating deposited with small powder (22 μm) is completely melted, whereas the coatings deposited with medium powder (33 μm) and large powder (57 μm) both contain abundant unmelted regions. Furthermore, the coating deposited with small powder has the lowest porosity (7.9%) but the lowest thermal conductivity (0.45 W·m⁻¹·K⁻¹).

Because the thermal-mechanical properties of nanostructured TBCs are obviously better than those of conventional coatings are, some researchers consider that the application of nanostructured EBCs to CMCs is very promising and can effectively solve the problem of the decline in the thermal cycle performance of EBCs under long-term service at ultrahigh temperatures [115–117]. At present, research on nanostructured EBCs is still in the initial phase, and these studies are being carried out mainly by the Harbin Institute of Technology [118] and Beijing Institute of Technology [119] in China. How to prepare nanostructured feedstock powder is the key to realizing nanostructured EBCs. Li *et al.* [52] used nanostructured feedstock powder with good sphericity and smooth surfaces after plasma treatment to prepare nanostructured $Yb_2Si_2O_7$ EBCs. The successfully prepared nanostructured $Yb_2Si_2O_7$ coating contains dense regions of complete melting and loose regions due to incomplete molten powder. However, a new phase of Yb_2SiO_5 appears in the coating due to the inevitable $Yb_2Si_2O_7$ phase decomposition at high temperatures. Guo *et al.* [119] successfully prepared nanostructured $Lu_2Si_2O_7$ feedstock powder via spray drying and prepared nanostructured $Lu_2Si_2O_7$ coatings via APS (Fig. 19). A comparison of the microstructures and properties of the nanostructured $Lu_2Si_2O_7$ coating and conventional $Lu_2Si_2O_7$ coating indicated that both coatings have dense and loose regions, but the pores and microcracks in the conventional $Lu_2Si_2O_7$ coating are coarser. The nanostructured $Lu_2Si_2O_7$ coating (7.6%±0.3%) has a lower porosity than the conventional $Lu_2Si_2O_7$ coating (11.3%±0.2%, 0.70–1.37 W·m⁻¹·K⁻¹) but a lower thermal conductivity (0.53–1.27 W·m⁻¹·K⁻¹).

In general, the meticulous and accurate adjustment of the morphology, internal structure, size and distribution of feedstock powder and many other key factors when preparing TBCs/EBCs is highly important for optimizing the comprehensive properties of coatings, such as the thermal conductivity, porosity, sintering resistance, and corrosion resistance.

3.3 Application of granulation technology for high-entropy ceramics in TBCs/EBCs

To improve the thermal and mechanical properties of TBCs/EBCs to meet the increasingly harsh service environment, many researchers have been devoted to applying high-entropy ceramics

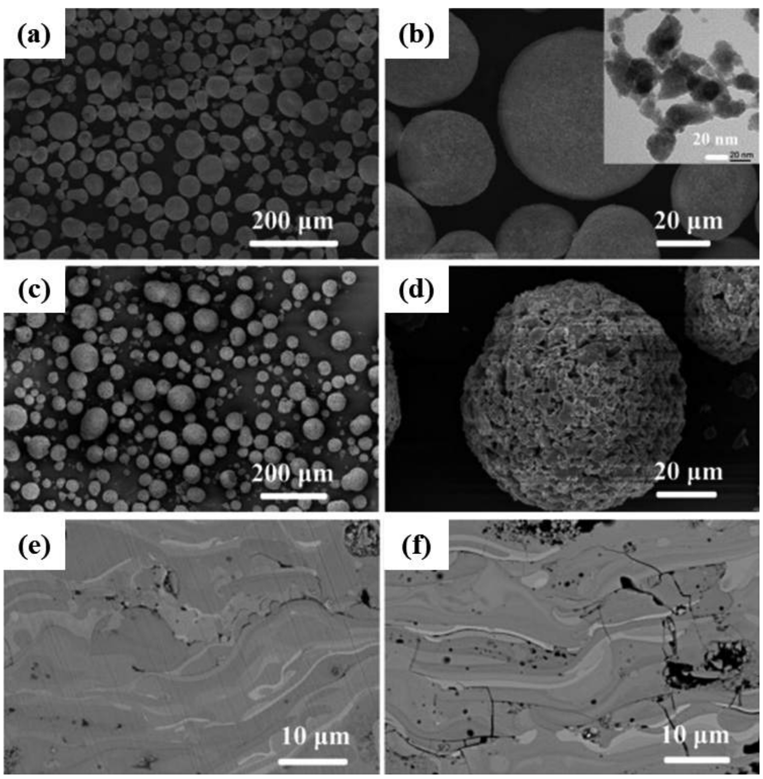

Fig. 19 SEM images of (a, b) nanostructured $Lu_2Si_2O_7$ feedstock powder and (c, d) conventional $Lu_2Si_2O_7$ feedstock powder. Cross-sectional morphologies of (e) nanostructured $Lu_2Si_2O_7$ coating and (b) conventional $Lu_2Si_2O_7$ coating. Reproduced with permission from Ref. [119], © Elsevier B.V. 2024.

in the TBC/EBC field [120,121], conforming TBCs/EBCs to low thermal conductivity, good thermal cycle stability, and excellent resistance to sintering and corrosion [122–124]. Currently, researchers have focused on two aspects to prepare high-entropy TBCs/EBCs with excellent comprehensive performance. On the one hand, it aims to find suitable chemical components to improve its phase stability at high temperatures and optimize its thermal and mechanical properties. Tu *et al.* [125] studied the resistance to CMAS corrosion of a $(La_{0.2}Nd_{0.2}Sm_{0.2}Eu_{0.2}Gd_{0.2})_2Zr_2O_7$ high-entropy ceramic at 1300 °C, and the results revealed that the resistance to CMAS corrosion of this high-entropy ceramic was significantly greater than that of the single rare-earth component ceramic $La_2Zr_2O_7$. Sun *et al.* [126] developed a new high-entropy disilicate $(Er_{0.25}Tm_{0.25}Yb_{0.25}Lu_{0.25})_2Si_2O_7$, which showed better resistance to water vapor corrosion at 1400 °C and superior resistance to CMAS corrosion at 1500 °C than did a single rare-earth component disilicate. These studies provide a theoretical basis for the future development of TBCs/EBCs, but because the focus is on the physical and chemical characteristics of the material itself, there is still a distance from practical application.

On the other hand, some researchers have begun to explore the structure and properties of high-entropy ceramics in coating states, promoting the application of high-entropy ceramics in the field of TBCs/EBCs. However, most high-entropy TBCs/EBCs reported in the literature were prepared via the spray drying method or agglomeration and sintering method, which were developed on the basis of binary chemical components decades ago [127,128]. In addition, only the flowability of feedstock powder is guaranteed to meet the requirements of spraying technology during the process of granulation, while the influence of the internal structure and external morphology of feedstock powder on the structure and properties of coatings has not received enough attention. Moreover, granulation technology is not optimized according to the characteristics of high-entropy ceramics. However, because the components of high-entropy ceramics are more complex, accurately determining the characteristics of such complex components by simply applying the spraying process parameters and granulation technology of single rare-earth component coatings is often difficult. Therefore, the advantages of high-entropy ceramics are that they cannot be fully utilized, which makes it difficult to effectively improve the comprehensive performance of the coating. In addition, feedstock powder with random configurations and structures exhibits unpredictable variations in both melting and solidification during the thermal spraying process. Thus, undesirable phase segregation, amorphous phase, and microstructure defects are often observed in as-received multicomponent ceramic coatings prepared via traditional granulation technology and thermal spraying parameters, leading to large differences in design life and practical performance [129].

The $(La_{0.35}Gd_{0.35}Y_{0.35}Sm_{0.35}Yb_{0.6})Zr_2O_7$ coating deposited by APS after spray drying can support 135±5 thermal cycles during thermal shock, which is 125% longer than that of the traditional YSZ coating. Moreover, it has better fracture toughness and the ability to inhibit the growth of thermally grown oxide (TGO), which improves the thermal shock resistance [130]. The original crystal structure tends to become unstable during high-temperature and rapid cooling, which is conducive to the formation and preservation of disordered fluorite structures [131,132]. The $(La_{0.35}Gd_{0.35}Y_{0.35}Sm_{0.35}Yb_{0.6})Zr_2O_7$ coating is also not exceptional. After spray drying, the powder exhibited fluorite and pyrochlore phases, whereas the deposited coating contained a single defective fluorite phase. Similarly, the $La_2(Zr_{0.2}Ce_{0.2}Hf_{0.2}Sn_{0.2}Ti_{0.2})_2O_7$ powder presents a pyrochlore structure after spray drying, but the coating prepared by APS presents a defective fluorite structure [133]. Similar problems exist with the top coat of EBCs. The weight loss rate of the new $(Lu_{0.2}Yb_{0.2}Er_{0.2}Tm_{0.2}Sc_{0.2})_2Si_2O_7$ coating prepared by APS after spray drying was only 0.2% after 100 h of water vapor corrosion at a high temperature of 1500 °C, indicating excellent resistance to water vapor corrosion [134]. Notably, three kinds of contrast can

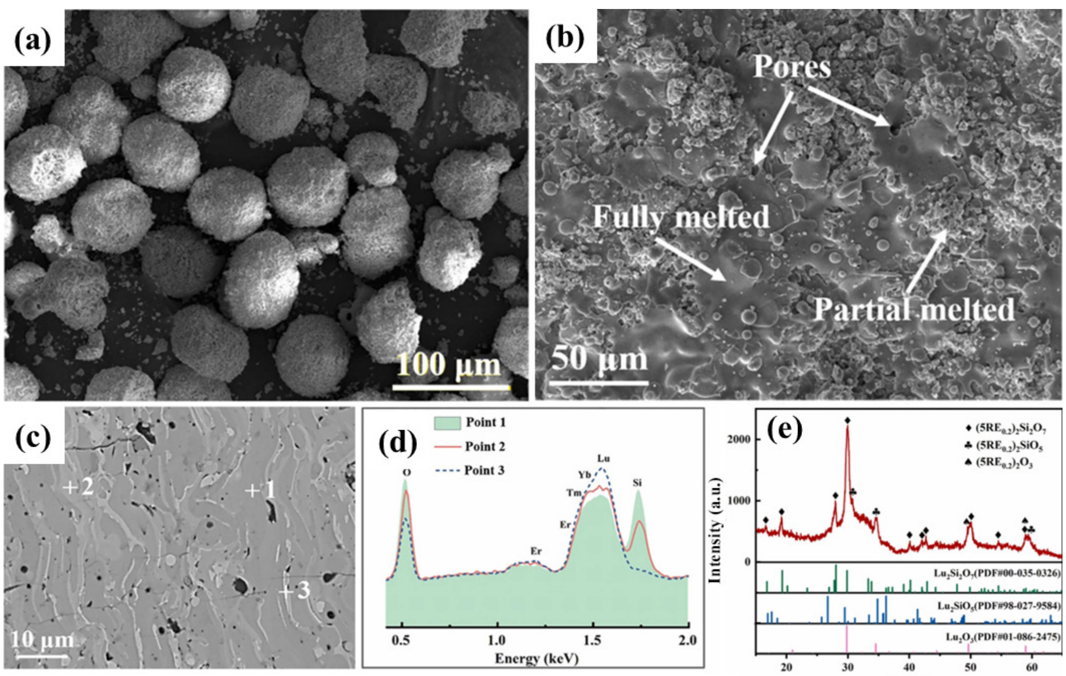

Fig. 20 (a) Morphology of $(Lu_{0.2}Yb_{0.2}Er_{0.2}Tm_{0.2}Sc_{0.2})_2Si_2O_7$ powder, (b) SEM image of deposited coating, (c) cross-section image of $(Lu_{0.2}Yb_{0.2}Er_{0.2}Tm_{0.2}Sc_{0.2})_2Si_2O_7$ coating, (d) EDS point scanning results of Points 1, 2, and 3 in (c), (e) XRD patterns of $(Lu_{0.2}Yb_{0.2}Er_{0.2}Tm_{0.2}Sc_{0.2})_2Si_2O_7$ coating. Reproduced with permission from Ref. [134], © Elsevier Ltd. 2023.

be observed in the prepared coating, as shown in Fig. 20, which is due to the phase decomposition that occurs during the spraying process. In addition to the main phase $(5RE_{0.2})_2Si_2O_7$, there are also phases of $(5RE_{0.2})_2SiO_5$ and $(5RE_{0.2})O_3$ in the coating because of the varying degrees of Si volatilization. The XRD diffraction peak becomes wide, indicating the existence of an amorphous phase, which is caused by the rapid cooling of the powder after melting during the spraying process. In addition, some vertical cracks are formed in the coating due to stress relaxation, providing infiltration paths for water vapor. Fan *et al.* [135] combined spray drying and APS to prepare $(Lu_{0.25}Yb_{0.25}Er_{0.25}Y_{0.25})_2SiO_5$ and $(Lu_{0.2}Yb_{0.2}Er_{0.2}Ho_{0.2}Y_{0.2})2)_2SiO_5$ coatings, which also have the problem of phase decomposition.

Because most studies focus on the physical and chemical characteristics of the material itself, ignoring the effects of the structure and morphology of feedstock powder as well as the spraying process on the structure and properties of coatings, the current studies on granulation technology and spraying processes suitable for high-entropy ceramics have not focused on the development of high-entropy TBCs/EBCs. There are still relatively few applications of the newly developed granulation technology and spraying process for high-entropy TBCs/EBCs because of their production efficiency and batch coast. Fortunately, some researchers have recently begun to address this problem by attempting to find suitable granulation technologies and spraying processes for high-entropy ceramics to optimize the coating structure, such as the burgeoning nanostructured coating, to fully exploit the advantages and properties of high-entropy ceramics. Yu *et al.* [74] utilized ESP-$(Sm_{0.2}Gd_{0.2}Dy_{0.2}Er_{0.2}Yb_{0.2})_2Zr_2O_7$ microspheres with different internal structures to prepare three kinds of nanostructured coatings via APS (Fig. 21). The results revealed that the thermal conductivity of the coating deposited with ESP microspheres with large 10 μm pores (0.80 $W·m^{-1}·K^{-1}$) was almost twice that of the coating deposited with ESP microspheres containing both large 10 μm pores and small 100 nm pores (0.41 $W·m^{-1}·K^{-1}$) at 1200 °C. The coatings prepared with ESP microspheres with different internal structures are all nanostructured, but the area of the dense region in the coatings prepared with ESP microspheres containing only large pores significantly increases. The optimization of the feedstock powder structure is highly important for the development of high-entropy TBCs/EBCs. The effects of feedstock powder on the thermal conductivity, thermal cycle lifetime, etc., of the deposited coatings cannot be ignored. The granulation and spraying technologies suitable for high-entropy ceramics applied in TBCs/EBCs still need further investigation.

Wang *et al.* [136] prepared integrated high-entropy TBCs/EBCs $(Yb_{0.25}Lu_{0.25}Er_{0.25}Y_{0.25})_2Si_2O_7$ and multilayer TBCs/EBCs $(LaMgAl_{11}O_{19}/Lu_2Si_2O_7)$ on the surface of SiC_f/SiC-CMCs by using APS after spray drying. The findings suggested that $(Yb_{0.25}Lu_{0.25}Er_{0.25}Y_{0.25})_2Si_2O_7$ has lower thermal conductivity and CET, better water vapor corrosion resistance, and a longer service lifetime. Two high-entropy rare-earth hafnate ceramics, $(La_{0.2}Gd_{0.2}Ho_{0.2}Er_{0.2}Tm_{0.2})_4Hf_3O_{12}$ and $(Yb_{0.2}Lu_{0.2}Ho_{0.2}Er_{0.2}Tm_{0.2})_4Hf_3O_{12}$, with defect fluorite structures, were also confirmed to exhibit lower CETs and thermal conductivities. $(Yb_{0.2}Lu_{0.2}Ho_{0.2}Er_{0.2}Tm_{0.2})_4Hf_3O_{12}$ can also rapidly react with CMAS to precipitate apatite and prevent CMAS from permeating at 1300 °C, indicating good application prospects in the TBC/EBC field [137,138]. This coating can be called the prototype of the current single material TBCs/EBCs, but there is still a certain gap in properties and other aspects from the real sense of TBCs/EBCs. The properties of several TBCs and EBCs prepared by different granulation technologies are summarized in Table 1.

Using the emerging granulation technology (e.g., microfluidics, electrostatic spraying) and spraying process (e.g., PS-PVD, SPS) in single-principal TBCs or EBCs for reference, as well as adjusting the internal structure and morphology of feedstock powder and spray process parameters to optimize the coating structure and achieve excellent comprehensive performance of high-entropy TBCs/EBCs, is one of the effective ways to explore and develop new high-entropy TBCs/EBCs in the future. Notably, the spraying process and parameter adjustment are largely based on the internal structure, external morphology, and particle size distribution of the feedstock powder.

4 Conclusions and prospects

Over 1600 °C, the working temperature of advanced gas turbines made of CMC material poses multiple challenges to the current zirconia-based top coat used in commercial TBCs. Blooming medium/high-entropy ceramics have shown great potential as candidates for advanced TBCs/EBCs owing to their prominent thermal and mechanical properties. The current research on medium-/high-entropy ceramics focuses on the specimen stage at the laboratory scale. Most feedstock powder used for medium/high-entropy TBCs/EBCs is prepared via traditional spray drying and wet chemistry technologies, which cannot fully

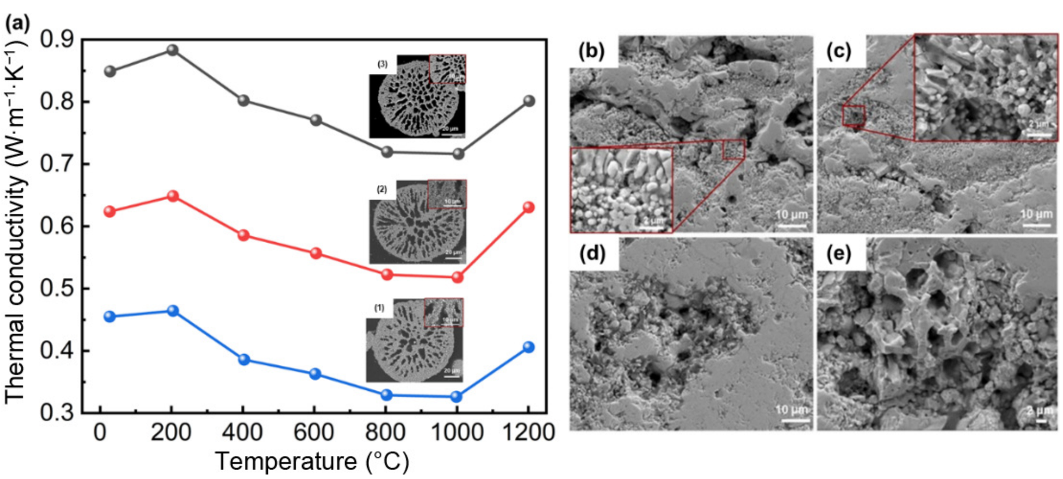

Fig. 21 (a) Thermal conductivity and (b–e) cross-sectional microstructures of coatings prepared from ESP microspheres with different internal structures, where coating (b) corresponds to structure (1) in (a), coating (c) corresponds to structure (2) in (a), and coatings (d, e) correspond to structure (3) in (a). Reproduced with permission from Ref. [74], © Elsevier Ltd. 2024.

Table 1 Comparison of the thermal and mechanical properties of TBCs/EBCs

Material	Granulation technology	Porosity (%)	Thermal conductivity ($W\cdot m^{-1}\cdot K^{-1}$)	Youngal conduct (GPa)	Fracture toughness ($MPa\cdot m^{1/2}$)
YSZ [71,100,110]	ESP	20.0	0.70	96	1.51–2.23
YSZ [71,75,77,79]	HOSP	12.2	1.10	110	1.80
YSZ [71,75,77]	A&S	15.1	1.22	100	—
YSZ [71,75,77,79]	F&C	7.6	1.31	125	—
$La_2(Zr_{0.75}Ce_{0.25})_2O_7$ [112]	Spray drying	15.0	0.65	—	—
$LaYbZr_2O_7$ [36]	ESP	7.9	0.45	—	—
$La_2Zr_2O_7$ [57,73]	ESP	—	0.52	—	—
$La_2Zr_2O_7$ [130]	Spray drying	19.3±0.9	—	—	0.86±0.06
$(LaGdYSmYb_{0.6})Zr_2O_7$ [130]	Spray drying	17.2±0.7	—	—	1.12±0.07
$(SmGdDyErYb)_2Zr_2O_7$ [74]	ESP	—	0.41	—	—
Lu_2SiO_5 [55,116] (nanosized)	Spray drying	—	0.78–1.20	149	—
$Lu_2Si_2O_7$ [119] (nanosized)	Spray drying	7.6±0.3	0.53–1.27	—	—
Yb_2SiO_5 [139] (nanosized)	Spray drying	8.9	0.71–1.22	—	1.21
Yb_2SiO_5 [139]	Spray drying	10.6	0.81–1.32	—	0.71
$(YbLuErY)_2Si_2O_7$ [136]	Spray drying	—	—	—	1.71
$(YbYLuHoEr)_2Si_2O_7$ [128]	Spray drying	—	0.67-0.98	—	—

exploit the advantages of multicomponent ceramics. The melting status of feedstock powder during heating depends on their density, sphericity, inner structure, and size, which strongly affect the microstructure and residual stress level of the deposited coatings. Feedstock powder with random configurations and structures exhibits unpredictable variations in both melting and solidification during the thermal spraying process. Thus, undesirable phase segregation, amorphous phase, and microstructure defects are often observed in as-received multicomponent ceramic coatings prepared via traditional granulation technology and thermal spraying parameters, leading to large differences in design life and practical performance. In summary, the theoretical knowledge and thermal spraying experience derived from granulation technologies in the context of binary ceramics hardly guide the performance optimization of medium/high-entropy ceramic coatings. Systematic investigations of multicomponent medium/high-entropy ceramic particle trajectories and temperature history in the context of basic phenomena governing momentum, heat, and mass exchange between the plasma and the particles can guide the optimization of feedstock powder fabricated via microfluidic techniques, which could greatly increase the manufacturing accuracy of thermally deposited coatings on both the composition and structure sides. The practical application and granulation technology suitable for high-entropy ceramic coatings still need further exploration. This review focuses only on the influence of feedstock powder on ceramic top coats utilized for thermal and environmental protection. Nevertheless, the bonding layer, material composition, and spraying technique synergistically play important roles in improving the comprehensive properties of TBCs/EBCs. It is necessary to thoroughly apply the existing research results to successfully prepare TBCs/EBCs that can be employed at temperatures above 1600 °C and have excellent long-term performance.

Acknowledgements

This work was supported by the Shanghai Pujiang Program (No. 2022PJD033), the Oceanic Interdisciplinary Program of Shanghai Jiao Tong University (No. SL2022MS013), and the Key R&D Program of Zhejiang (No. 2024SSYS0085). We thank Professor Xueqiang Cao from Wuhan University of Technology and Dr. Micheal Wang for carefully supervising the writing logic throughout the manuscript.

Declaration of competing interest

The authors have no competing interests to declare that are relevant to the content of this article. The author Chunlei Wan is the Associate Editor of this journal. The authors Jing Feng and Lei Guo are Editorial Committee members of this journal.

References

[1] Information on https://baijiahao.baidu.com/s?id=1804336916860423947&wfr=spider&for=pc.

[2] Zhu DM, Miller R, Fox D. Thermal and Environmental barrier coating development for advanced propulsion engine systems. In: Proceedings of the 48th AIAA/ASME/ASCE/AHS/ASC Structures, Structural Dynamics, and Materials Conference, 2007: 2130.

[3] Krenkel W, Berndt F. C/C–SiC composites for space applications and advanced friction systems. *Mat Sci Eng A-Struct* 2005, **412**: 177–181.

[4] Curtin WA. Theory of mechanical properties of ceramic–matrix composites. *J Am Ceram Soc* 1991, **74**: 2837–2845.

[5] Zhu DM. NASA's advanced environmental barrier coatings development for SiC/SiC ceramic matrix composites: Understanding CMAS degradations and resistance. In: Proceedings of Thermal Barrier Coatings IV Conference, 2014.

[6] Opila EJ, Hann Jr RE. Paralinear oxidation of CVD SiC in water vapor. *J Am Ceram Soc* 1997, **80**: 197–205.

[7] Dong N, Luan XG, Cheng LF. Corrosion of C/SiC composite in water vapor and Na_2SO_4 vapor. *Sci Eng Compos Mater* 2008, **15**: 121–129.

[8] Ridley M, Kane K, Lance M, *et al.* Steam oxidation and microstructural evolution of rare earth silicate environmental barrier coatings. *J Am Ceram Soc* 2023, **106**: 613–620.

[9] Eaton HE, Linsey GD. Accelerated oxidation of SiC CMC's by water vapor and protection via environmental barrier coating approach. *J Eur Ceram Soc* 2002, **22**: 2741–2747.

[10] Turcer LR, Padture NP. Towards multifunctional thermal environmental barrier coatings (TEBCs) based on rare-earth

pyrosilicate solid-solution ceramics. *Scripta Mater* 2018, **154**: 111–117.

[11] Zhu DM. Advanced environmental barrier coatings for SiC/SiC ceramic matrix composite turbine components. In: *Engineered Ceramics: Current Status and Future Prospects*. Ohji T, Singh M, Eds. Hoboken: John Wiley & Sons, Inc., 2015: 187–202.

[12] Poerschke DL, Hass DD, Eustis S, *et al.* Stability and CMAS resistance of ytterbium-silicate/hafnate EBCs/TBC for SiC composites. *J Am Ceram Soc* 2015, **98**: 278–286.

[13] Chen HF, Zhang C, Liu YC, *et al.* Recent progress in thermal/environmental barrier coatings and their corrosion resistance. *Rare Metals* 2020, **39**: 498–512.

[14] Zhang Q, Zhang XQ, Ma Z, *et al.* Water vapor and CMAS corrosion tests of Y_2SiO_5/Si thermal and environmental barrier coating. *Heliyon* 2022, **8**: e10262.

[15] Information on https://ntrs.nasa.gov/citations/20050192261.

[16] Tian ZL, Zheng LY, Wang JM, *et al.* Theoretical and experimental determination of the major thermo-mechanical properties of RE_2SiO_5 (RE = Tb, Dy, Ho, Er, Tm, Yb, Lu, and Y) for environmental and thermal barrier coating applications. *J Eur Ceram Soc* 2016, **36**: 189–202.

[17] Clarke DR, Oechsner M, Padture NP. Thermal-barrier coatings for more efficient gas-turbine engines. *MRS Bull* 2012, **37**: 891–898.

[18] Guo FW, Zhang RJ, Xing C, *et al.* Review on thermal spraying powder with hierarchy pore structure and a new generation of long-life thermal barrier coating materials. *J Aeronaut Mater* 2023, **43**: 1–16. (in Chinese)

[19] Thakare JG, Pandey C, Mahapatra MM, *et al.* Thermal barrier coatings—A state of the art review. *Met Mater Int* 2021, **27**: 1947–1968.

[20] Guo L, He WT, Chen WB, *et al.* Progress on high-temperature protective coatings for aero-engines. *Surf Sci Technol* 2023, **1**: 6.

[21] Mondal K, Nuñez III L, Downey CM, *et al.* Thermal barrier coatings overview: Design, manufacturing, and applications in high-temperature industries. *Ind Eng Chem Res* 2021, **60**: 6061–6077.

[22] Liu QM, Huang SZ, He AJ. Composite ceramics thermal barrier coatings of yttria stabilized zirconia for aero-engines. *J Mater Sci Technol* 2019, **35**: 2814–2823.

[23] Zhang XF, Zhou KS, Chang F, *et al.* Yttria-stabilized-zirconia hollow spheres prepared by atmospheric plasma spray. *Particuology* 2014, **14**: 57–62.

[24] Wang Y, Hsu PF. Microstructure modifications to enhance the scattering coefficient of porous yttria-stabilized zirconia coatings. *J Therm Spray Techn* 2024, **33**: 181–194.

[25] Zhang H, Chen Y, Li L, *et al.* Unraveling the CMAS corrosion mechanism of APS high-yttria-stabilized zirconia thermal barrier coatings. *J Eur Ceram Soc* 2024, **44**: 5154–5165.

[26] Velasco JHR, Petrosky K, Kilaz G, *et al.* Thermochemical interaction of biofuel impurities with yttria-stabilized zirconia thermal barrier coatings. *Ceram Int* 2021, **47**: 24675–24682.

[27] Pakseresht A, Sharifianjazi F, Esmaeilkhanian A, *et al.* Failure mechanisms and structure tailoring of YSZ and new candidates for thermal barrier coatings: A systematic review. *Mater Design* 2022, **222**: 111044.

[28] Qin SY, Cao HT, Gao ZH, *et al.* A new Al_2O_3-protected EB-PVD TBC with superior CMAS resistance. *Adv Sci* 2024, **11**: 2305479.

[29] Lin GQ, Wang YL, Yang LX, *et al.* CMAS corrosion behavior of a novel high entropy $(Nd_{0.2}Gd_{0.2}Y_{0.2}Er_{0.2}Yb_{0.2})_2Zr_2O_7$ thermal barrier coating materials. *Corros Sci* 2023, **224**: 111529.

[30] Deng SX, He G, Yang ZC, *et al.* Calcium–magnesium–alumina–silicate (CMAS) resistant high entropy ceramic $(Y_{0.2}Gd_{0.2}Er_{0.2}Yb_{0.2}Lu_{0.2})_2Zr_2O_7$ for thermal barrier coatings. *J Mater Sci Technol* 2022, **107**: 259–265.

[31] Ball JAJ, Martins JF, Brewster G, *et al.* An investigation into RESZ (RE = Yb, Er, Gd, Sm) materials for CMAS resistance in thermal barrier coatings. *J Eur Ceram Soc* 2024, **44**: 3734–3746.

[32] Yao Y, Yang F, Zhao XF. Multicomponent high-entropy Zr–Y–Yb–Ta–Nb–O oxides for next-generation thermal barrier coating applications. *J Am Ceram Soc* 2022, **105**: 35–43.

[33] Wang KL, Zhu JP, Wang HL, *et al.* Air plasma-sprayed high-entropy $(Y_{0.2}Yb_{0.2}Lu_{0.2}Eu_{0.2}Er_{0.2})_3Al_5O_{12}$ coating with high thermal protection performance. *J Adv Ceram* 2022, **11**: 1571–1582.

[34] Liu DB, Shi BL, Geng LY, *et al.* High-entropy rare-earth zirconate ceramics with low thermal conductivity for advanced thermal-barrier coatings. *J Adv Ceram* 2022, **11**: 961–973.

[35] Arai Y, Inoue R. Detection of small delamination in mullite/Si/SiC model EBC system by pulse thermography. *J Adv Ceram* 2019, **8**: 438–447.

[36] Yu YL, Zhang P, Liu XY, *et al.* Effect of feedstock powder size on the microstructure and thermal conductivity of quasi-eutectic $LaYbZr_2O_7$ TBCs. *Ceram Int* 2024, **50**: 13684–13689.

[37] Wang HY, Zhang J, Sun LC, *et al.* Microstructure and phase composition evolution of dual-phase ytterbium silicate coatings plasma sprayed from stoichiometric $Yb_2Si_2O_7$ feedstock powder. *Surf Coat Tech* 2022, **437**: 128373.

[38] Richards BT, Zhao HB, Wadley HNG. Structure, composition, and defect control during plasma spray deposition of ytterbium silicate coatings. *J Mater Sci* 2015, **50**: 7939–7957.

[39] Łatka L. Thermal barrier coatings manufactured by suspension plasma spraying—A review. *Adv Mater Sci* 2018, **18**: 95–117.

[40] Goral M, Kotowski S, Nowotnik A, *et al.* PS-PVD deposition of thermal barrier coatings. *Surf Coat Tech* 2013, **237**: 51–55.

[41] Shi MC, Xue ZL, Zhang ZY, *et al.* Effect of spraying powder characteristics on mechanical and thermal shock properties of plasma-sprayed YSZ thermal barrier coating. *Surf Coat Tech* 2020, **395**: 125913.

[42] Sharma A, Witz G, LeCreux C, *et al.* High heat flux burner-rig testing of 8YSZ thermal barrier coatings: Influence of the powder feedstock. *J Eur Ceram Soc* 2022, **42**: 7267–7274.

[43] Wang JS, Sun JB, Zhang H, *et al.* Effect of spraying power on microstructure and property of nanostructured YSZ thermal barrier coatings. *J Alloys Compd* 2018, **730**: 471–482.

[44] Sun QY, Liu T, Wen TP, *et al.* Ethanol-induced formation of precursor for 8 mol% Yttria-stabilized zirconia: Towards the production of well-dispersed, easily sintering, and high-conductivity nano-powders. *J Eur Ceram Soc* 2023, **43**: 6934–6945.

[45] Esmaeilkhanian AH, Sharifianjazi F, Ahmadi E, *et al.* Thermal barrier coating with improved durability: An overview of doped, nanostructured, multilayered, and gradient-structured zirconia-based thermal barrier coatings. *Mater Today Commun* 2023, **37**: 107514.

[46] Xue ZL, Zhu Y, Yu HY, *et al.* Nano-agglomerated powder and thermal shock cycling property of 8YSZ nano-structured thermal barrier coating. *Surf Coat Tech* 2022, **433**: 128173.

[47] Ghoshal A, Murugan M, Walock MJ, *et al.* Molten particulate impact on tailored thermal barrier coatings for gas turbine engine. *J Eng Gas Turb Power* 2018, **140**: 022601.

[48] Salam Hamdy A. Corrosion protection performance via nano-coatings technologies. *Recent Pat Mater Sci* 2010, **3**: 258–267.

[49] Lu XR, Yuan JY, Li G, *et al.* Microstructures, thermophysical properties and thermal cyclic behaviors of Nd_2O_3 and Sc_2O_3 Co-doped $LaMgAl_{11}O_{19}$ thermal barrier coating deposited by plasma spraying. *Ceram Int* 2022, **48**: 36539–36555.

[50] Guo FW, Xing C, Wang GW, *et al.* Hollow ceramic microspheres prepared by combining electro-spraying with non-solvent induced phase separation method: A promising feedstock for thermal barrier coatings. *Mater Design* 2018, **139**: 343–350.

[51] Kang Y, Liu MJ, Chen L, *et al.* YSZ/Ni double-shell powder via surface electroless deposition tuned by an active kinetic model. *Int J Appl Ceram Tec* 2023, **20**: 2137–2147.

[52] Li BX, Zhang XD, Zhang ZG, *et al.* Preparation and

characterization of a novel nanostructured $Yb_2Si_2O_7$ feedstock used for plasma-sprayed environmental barrier coatings. *Ceram Int* 2023, **49**: 10897–10905.
[53] Xiao F, Zhang XD, Li BX, *et al.* Nanostructured Yb_2SiO_5/mullite–SiC/Si environmental barrier coating with long-term stability at 1250 °C. *Ceram Int* 2024, **50**: 27974–27983.
[54] Zhou FF, Guo DH, Xu BS, *et al.* Novel controllable solid/hollow T'-YSZ nanostructured powders for additive manufacturing. *Ceram Int* 2022, **48**: 24125–24128.
[55] Guo DH, Liu J, Shi JZ, *et al.* Synthesis and characterization of single-phase X2-Lu_2SiO_5 nanostructured feedstocks for advanced plasma-sprayed environmental barrier coatings. *Surf Coat Tech* 2024, **476**: 130230.
[56] Xing C, Yi MY, Zhang X, *et al.* Compression strength and fracture mechanism of a hierarchical porous yttria-stabilized zirconia microsphere prepared using electro-spraying associated with phase inversion technique. *Ceram Int* 2021, **47**: 18132–18139.
[57] Yu YL, Guo FW, Xing C, *et al.* Thermal properties of hierarchical YSZ and LZO ceramic microspheres with multi-scaled voids investigated by using theoretical, experimental and simulation methods. *Adv Powder Technol* 2022, **33**: 103879.
[58] Guo HB, Murakami H, Kuroda S. Effect of hollow spherical powder size distribution on porosity and segmentation cracks in thermal barrier coatings. *J Am Ceram Soc* 2006, **89**: 3797–3804.
[59] Buelna G, Lin YS. Sol–gel-derived mesoporous γ-alumina granules. *Micropor Mesopor Mat* 1999, **30**: 359–369.
[60] Song J, Kim B, Park D, *et al.* Fabrications of spherical alumina particles by controlling process parameters in a transferred arc plasma system. *Ceram Int* 2020, **46**: 21225–21232.
[61] Lou XW, Archer LA, Yang ZC. Hollow micro-/nanostructures: Synthesis and applications. *Adv Mater* 2008, **20**: 3987–4019.
[62] Hu J, Chen M, Fang XS, *et al.* Fabrication and application of inorganic hollow spheres. *Chem Soc Rev* 2011, **40**: 5472–5491.
[63] Yu M, Zhou KC, Zhang Y, *et al.* Porous Al_2O_3 microspheres prepared by a novel ice-templated spray drying technique. *Ceram Int* 2014, **40**: 1215–1219.
[64] Nouri A, Sola A. Powder morphology in thermal spraying. *J Adv Manuf & Process* 2019, **1**: 10020.
[65] Stunda-Zujeva A, Irbe Z, Berzina-Cimdina L. Controlling the morphology of ceramic and composite powders obtained via spray drying—A review. *Ceram Int* 2017, **43**: 11543–11551.
[66] Kim DJ, Jung JY. Granule performance of zirconia/alumina composite powders spray-dried using polyvinyl pyrrolidone binder. *J Eur Ceram Soc* 2007, **27**: 3177–3182.
[67] Zhu RB, Zou JP, Mao J, *et al.* A comparison between novel $Gd_2Zr_2O_7$ and $Gd_2Zr_2O_7$/YSZ thermal barrier coatings fabricated by plasma spray-physical vapor deposition. *Rare Metals* 2021, **40**: 2244–2253.
[68] Luo GS, Wang K, Wang PJ, *et al.* Advances in polymer synthesis in microreactors. *CIESC J* 2014, **65**: 2563–2573. (in Chinese)
[69] Liang SS, Li J, Li XM, *et al.* Microfluidic fabrication of ceramic microspheres with controlled morphologies. *J Am Ceram Soc* 2018, **101**: 3787–3796.
[70] Chu LY, Utada AS, Shah RK, *et al.* Controllable monodisperse multiple emulsions. *Angew Chem-Ger Edit* 2007, **46**: 8970–8974.
[71] Zou ZH, Xing C, He LM, *et al.* A highly strain and damage-tolerant thermal barrier coating fabricated by electro-sprayed zirconia hollow spheres. *J Am Ceram Soc* 2018, **101**: 4375–4386.
[72] Zhang RJ, Guo FW, Zhang X, *et al.* ZrB_2–SiC spiral fibers prepared by combining liquid rope effect with non-solvent-induced phase separation method: A promising toughening material for ultra-high temperature ceramics. *J Adv Ceram* 2023, **12**: 132–144.
[73] Yu YL, Zhang X, Guo FW, *et al.* Enhanced near infrared reflectivity in hierarchical porous $La_2Zr_2O_7$ microspheres produced by electro-spraying assisted phase inversion method. *Opt Mater* 2021, **118**: 111270.
[74] Yu YL, Zhang P, Zhang XF, *et al.* Formation mechanism of an ultra-low thermal conductivity thermal barrier coating deposited using biomimetic hierarchical porous microspheres. *J Eur Ceram Soc* 2025, **45**: 116862.
[75] Kulkarni A, Wang Z, Nakamura T, *et al.* Comprehensive microstructural characterization and predictive property modeling of plasma-sprayed zirconia coatings. *Acta Mater* 2003, **51**: 2457–2475.
[76] Allen AJ, Ilavsky J, Long GG, *et al.* Microstructural characterization of yttria-stabilized zirconia plasma-sprayed deposits using multiple small-angle neutron scattering. *Acta Mater* 2001, **49**: 1661–1675.
[77] Chi WG, Sampath S, Wang H. Microstructure–thermal conductivity relationships for plasma-sprayed yttria-stabilized zirconia coatings. *J Am Ceram Soc* 2008, **91**: 2636–2645.
[78] Bertrand G, Bertrand P, Roy P, *et al.* Low conductivity plasma sprayed thermal barrier coating using hollow psz spheres: Correlation between thermophysical properties and microstructure. *Surf Coat Tech* 2008, **202**: 1994–2001.
[79] Dwivedi G, Viswanathan V, Sampath S, *et al.* Fracture toughness of plasma-sprayed thermal barrier ceramics: Influence of processing, microstructure, and thermal aging. *J Am Ceram Soc* 2014, **97**: 2736–2744.
[80] Tan Y, Longtin JP, Sampath S, *et al.* Effect of the starting microstructure on the thermal properties of as-sprayed and thermally exposed plasma-sprayed YSZ coatings. *J Am Ceram Soc* 2009, **92**: 710–716.
[81] Ercan B, Bowman KJ, Trice RW, *et al.* Effect of initial powder morphology on thermal and mechanical properties of stand-alone plasma-sprayed 7 wt% Y_2O_3–ZrO_2 coatings. *Mat Sci Eng A-Struct* 2006, **435**: 212–220.
[82] Ilavsky J, Stalick JK. Phase composition and its changes during annealing of plasma-sprayed YSZ. *Surf Coat Tech* 2000, **127**: 120–129.
[83] Liu MJ, Zhang M, Zhang XF, *et al.* Transport and deposition behaviors of vapor coating materials in plasma spray-physical vapor deposition. *Appl Surf Sci* 2019, **486**: 80–92.
[84] Avcı A, Karabaş M, Eker AA, *et al.* Improvement of CMAS resistance of laser glazed and nano-modified YSZ thermal barrier coatings. *Ceram Int* 2024, **50**: 9985–9999.
[85] Busso EP, Wright L, Evans HE, *et al.* A physics-based life prediction methodology for thermal barrier coating systems. *Acta Mater* 2007, **55**: 1491–1503.
[86] Mercer C, Faulhaber S, Evans AG, *et al.* A delamination mechanism for thermal barrier coatings subject to calcium–magnesium–alumino–silicate (CMAS) infiltration. *Acta Mater* 2005, **53**: 1029–1039.
[87] Yan Z, Guo L, Li ZH, *et al.* Effects of laser glazing on CMAS corrosion behavior of Y_2O_3 stabilized ZrO_2 thermal barrier coatings. *Corros Sci* 2019, **157**: 450–461.
[88] Ma X, Ruggiero P, Wildridge G. Evaluation of CMAS resistance and failure behavior for phase composite thermal barrier coatings. *J Therm Spray Techn* 2023, **32**: 693–705.
[89] Guo L, Gao Y, Ye FX, *et al.* CMAS corrosion behavior and protection method of thermal barrier coatings for aeroengine. *Acta Metall Sin* 2021, **57**: 1184–1198. (in Chinese)
[90] Wang JS, Lu XJ, Shu CX, *et al.* CMAS corrosion resistance of YSZ thermal barrier coatings enhanced by Pt–Al films. *Ceram Int* 2024, **50**: 5111–5120.
[91] Peng H, Wang L, Guo L, *et al.* Degradation of EB-PVD thermal barrier coatings caused by CMAS deposits. *Prog Nat Sci-Mater* 2012, **22**: 461–467.
[92] Wu J, Guo HB, Abbas M, *et al.* Evaluation of plasma sprayed YSZ thermal barrier coatings with the CMAS deposits infiltration using impedance spectroscopy. *Prog Nat Sci-Mater* 2012, **22**: 40–47.
[93] Wang YL, Deng CG, Zhan ZL, *et al.* Thermal shock resistance and failure mechanism of CMAS deposited PS-PVD 7YSZ coating. *Heat Treat Met* 2017, **42**: 175–179. (in Chinese)

[94] Li X, Wang X, Niu SP, *et al.* Reactive deposition of CYSZ coatings using PS-PVD technology. *J Eur Ceram Soc* 2024, **44**: 6071–6081.
[95] Wei ZY, Meng GH, Chen L, *et al.* Progress in ceramic materials and structure design toward advanced thermal barrier coatings. *J Adv Ceram* 2022, **11**: 985–1068.
[96] Mauer G, Hospach A, Vaßen R. Process development and coating characteristics of plasma spray-PVD. *Surf Coat Tech* 2013, **220**: 219–224.
[97] Liu SH, Trelles JP, Murphy AB, *et al.* Low-pressure plasma-induced physical vapor deposition of advanced thermal barrier coatings: Microstructures, modelling and mechanisms. *Mater Today Phys* 2021, **21**: 100481.
[98] Jia F, Gao LH, Yu YG, *et al.* Influence of YSZ powder characteristics on the morphology of PS-PVD thermal barrier coatings. In: Thermal Spray 2019: Proceedings from the International Thermal Spray Conference, 2019: 975–980.
[99] Yin JA, Liu M, Zhang XF, *et al.* 8YSZ nano agglomeration powder prepared by spray-drying for PS-PVD. *Surf Technol* 2018, **47**: 275–282. (in Chinese)
[100] Zhang RJ, Zhang X, Xing C, *et al.* Preparation of long-lifetime thermal barrier coatings and toughening mechanism by using hierarchy structured zirconia-based microspheres. *J Eur Ceram Soc* 2021, **41**: 4625–4636.
[101] Lima RS, Kucuk A, Berndt CC. Bimodal distribution of mechanical properties on plasma sprayed nanostructured partially stabilized zirconia. *Mat Sci Eng A-Struct* 2002, **327**: 224–232.
[102] Lima RS, Marple BR. Thermal spray coatings engineered from nanostructured ceramic agglomerated powders for structural, thermal barrier and biomedical applications: A review. *J Therm Spray Techn* 2007, **16**: 40–63.
[103] Lima RS, Marple BR. Nanostructured YSZ thermal barrier coatings engineered to counteract sintering effects. *Mat Sci Eng A-Struct* 2008, **485**: 182–193.
[104] Kusano E, Kitagawa M, Satoh A, *et al.* Hardness of compositionally nano-modulated TiN films. *Nanostruct Mater* 1999, **12**: 807–810.
[105] Hernandez-Lopez JL, Bauer RE, Chang WS, *et al.* Functional polymers as nanoscopic building blocks. *Mater Sci Eng C* 2003, **23**: 267–274.
[106] Zhou CG, Wang N, Wang ZB, *et al.* Thermal cycling life and thermal diffusivity of a plasma-sprayed nanostructured thermal barrier coating. *Scripta Mater* 2004, **51**: 945–948.
[107] Ghasemi R, Vakilifard H. Plasma-sprayed nanostructured YSZ thermal barrier coatings: Thermal insulation capability and adhesion strength. *Ceram Int* 2017, **43**: 8556–8563.
[108] Liang B, Ding CX. Thermal shock resistances of nanostructured and conventional zirconia coatings deposited by atmospheric plasma spraying. *Surf Coat Tech* 2005, **197**: 185–192.
[109] Lima RS, Kucuk A, Berndt CC. Integrity of nanostructured partially stabilized zirconia after plasma spray processing. *Mat Sci Eng A-Struct* 2001, **313**: 75–82.
[110] Xing C, Yi MY, Shan X, *et al.* Sintering behavior of a nanostructured thermal barrier coating deposited using electro-sprayed particles. *J Am Ceram Soc* 2020, **103**: 7267–7282.
[111] Zhou FF, Liu M, Deng CM, *et al.* Nanostructured $La_2(Zr_{0.75}Ce_{0.25})_2O_7$ spherical feedstocks for plasma sprayed ultra-high temperature thermal barrier coatings. *Surf Technol* 2020, **49**: 98–103,112. (in Chinese)
[112] Yang P, An YL, Zhao D, *et al.* Structure evolution, thermal properties and sintering resistance of promising thermal barrier coating material $La_2(Zr_{0.75}Ce_{0.25})_2O_7$. *Ceram Int* 2020, **46**: 20652–20663.
[113] Zhao YL, Wen JH, Peyraut F, *et al.* Porous architecture and thermal properties of thermal barrier coatings deposited by suspension plasma spray. *Surf Coat Tech* 2020, **386**: 125462.
[114] Arai M, Ochiai H, Suidzu T. A novel low-thermal-conductivity plasma-sprayed thermal barrier coating controlled by large pores. *Surf Coat Tech* 2016, **285**: 120–127.
[115] Zheng T, Xu BS, Wang S, *et al.* Microstructure and nanomechanical properties of plasma-sprayed nanostructured Yb_2SiO_5 environmental barrier coatings. *J Am Ceram Soc* 2023, **106**: 2666–2678.
[116] Guo DH, Xu BS, Shi JZ, *et al.* Nanomechanical characterization of nanostructured Lu_2SiO_5 environmental barrier coatings by nano-indentation. *Surf Coat Tech* 2024, **477**: 130317.
[117] Guo DH, Peng XC, Shi BL, *et al.* Bimodal nanomechanical performance of nanostructured $Lu_2Si_2O_7$ environmental barrier coating. *Ceram Int* 2024, **50**: 27635–27638.
[118] Xiao F, Yan MF, Wang Y, *et al.* Water vapor corrosion behaviours of nanostructured Yb_2O_3–Yb_2SiO_5/mullite/Si environmental barrier coatings. *Ceram Int* 2025, **51**: 279–289.
[119] Guo DH, Shi JZ, Shi BL, *et al.* Comparison of thermal properties of conventional and nanostructured $Lu_2Si_2O_7$ environmental barrier coatings. *Surf Interfaces* 2024, **51**: 104799.
[120] Gild J, Wright A, Quiambao-Tomko K, *et al.* Thermal conductivity and hardness of three single-phase high-entropy metal diborides fabricated by borocarbothermal reduction and spark plasma sintering. *Ceram Int* 2020, **46**: 6906–6913.
[121] Song D, Song T, Paik U, *et al.* Glass-like thermal conductivity in mass-disordered high-entropy $(Y,Yb)_2(Ti,Zr,Hf)_2O_7$ for thermal barrier material. *Mater Design* 2021, **210**: 110059.
[122] Zhao ZF, Xiang HM, Dai FZ, *et al.* $(La_{0.2}Ce_{0.2}Nd_{0.2}Sm_{0.2}Eu_{0.2})_2Zr_2O_7$: A novel high-entropy ceramic with low thermal conductivity and sluggish grain growth rate. *J Mater Sci Technol* 2019, **35**: 2647–2651.
[123] Luo XW, Huang S, Huang RQ, *et al.* Phase evolution, thermophysical and mechanical properties of high-entropy $(Ce_{0.2}Nd_{0.2}Sm_{0.2}Eu_{0.2}Yb_{0.2})_2Zr_2O_7$ ceramic for advanced thermal barrier coatings. *J Eur Ceram Soc* 2024, **44**: 2452–2459.
[124] Zhang WC, Guo FW, Zhang RJ, *et al.* A simple route to synthesize high-entropy carbide $(Hf_{0.2}Zr_{0.2}Ti_{0.2}Ce_{0.2}La_{0.2})C_{1-\delta}$ nanoparticles with large covalent radius difference. *Ceram Int* 2023, **49**: 38566–38574.
[125] Tu TZ, Liu JX, Zhou L, *et al.* Graceful behavior during CMAS corrosion of a high-entropy rare-earth zirconate for thermal barrier coating material. *J Eur Ceram Soc* 2022, **42**: 649–657.
[126] Sun LC, Luo YX, Tian ZL, *et al.* High temperature corrosion of $(Er_{0.25}Tm_{0.25}Yb_{0.25}Lu_{0.25})_2Si_2O_7$ environmental barrier coating material subjected to water vapor and molten calcium–magnesium–aluminosilicate (CMAS). *Corros Sci* 2020, **175**: 108881.
[127] Lan YW, Cui JG, Dai BX, *et al.* One pot synthesis of high entropy rare earth zirconate ceramics with low thermal conductivity for high performance thermal-barrier coatings. *Mater Sci Eng B-Adv* 2024, **301**: 117186.
[128] Chen ZY, Lin CC, Zheng W, *et al.* A high-entropy $(Yb_{0.2}Y_{0.2}Lu_{0.2}Ho_{0.2}Er_{0.2})_2Si_2O_7$ environmental barrier coating prepared by atmospheric plasma-spray. *Ceram Int* 2023, **49**: 11323–11333.
[129] Zhang XD, Liang YF, Song Y, *et al.* Research progress of high entropy rare earth oxide thermal barrier coating materials. *Mater Prot* 2024, **57**: 15–27.
[130] Chen Z, Cui XF, Wang X, *et al.* Novel high-entropy $(La_{0.35}Gd_{0.35}Y_{0.35}Sm_{0.35}Yb_{0.6})Zr_2O_7$ thermal barrier coatings: Thermal cycling performance and failure behavior. *Ceram Int* 2024, **50**: 54716–54727.
[131] Zhou L, Li F, Liu JX, *et al.* High-entropy thermal barrier coating of rare-earth zirconate: A case study on $(La_{0.2}Nd_{0.2}Sm_{0.2}Eu_{0.2}Gd_{0.2})_2Zr_2O_7$ prepared by atmospheric plasma spraying. *J Eur Ceram Soc* 2020, **40**: 5731–5739.
[132] Zhou L, Huang ZY, Qi JQ, *et al.* Thermal-driven fluorite–pyrochlore–fluorite phase transitions of $Gd_2Zr_2O_7$

ceramics probed in large range of sintering temperature. *Metall Mater Trans A* 2016, **47**: 623–630.
[133] Zhang DB, Yu Y, Feng XL, *et al*. Thermal barrier coatings with high-entropy oxide as a top coat. *Ceram Int* 2022, **48**: 1349–1359.
[134] Chen GH, Zhang YL, Guo XT, *et al*. Microstructure and water corrosion behavior of $(Lu_{0.2}Yb_{0.2}Er_{0.2}Tm_{0.2}Sc_{0.2})_2Si_2O_7$ high-entropy rare-earth disilicate coating for SiC coated C/C composites. *J Eur Ceram Soc* 2023, **43**: 3647–3657.
[135] Fan D, Zhong X, Zhang ZZ, *et al*. Interaction of high-entropy rare-earth monosilicate environmental barrier coatings subjected to corrosion by calcium–magnesium–alumino–silicate melts. *Corros Sci* 2022, **207**: 110564.
[136] Wang ZT, Dong SJ, Mao CY, *et al*. Properties of $(Yb_{0.25}Lu_{0.25}Er_{0.25}Y_{0.25})_2Si_2O_7$ high entropy silicate thermal environmental barrier coating. *J Chin Soc Rare Earths* 2024, **42**: 752–761. (in Chinese)
[137] Hu WP, Lei YM, Zhang J, *et al*. Mechanical and thermal properties of $RE_4Hf_3O_{12}$ (RE = Ho, Er, Tm) ceramics with defect fluorite structure. *J Mater Sci Technol* 2019, **35**: 2064–2069.
[138] Hu WP, Zhang GH, Lei YM, *et al*. Mechanical and thermal properties of δ-$RE_4Hf_3O_{12}$ (RE = Yb, Lu). *Int J Appl Ceram Tec* 2023, **20**: 833–841.
[139] Zheng T, Wang S, Xu BS, *et al*. A study of fracture toughness and thermal property of nanostructured Yb_2SiO_5 environmental barrier coatings. *J Mater Res Technol* 2023, **26**: 4436–4443.